Science of the Total Environment 833 (2022) 155068

Contents lists available at ScienceDirect

Science of the Total Environment

journal homepage: www.elsevier.com/locate/scitotenv

Anthropogenic influence on surface changes at the Olivares glaciers; Central Chile

Martina Barandun [a,b,*], Claudio Bravo [c], Bernard Grobety [d], Theo Jenk [a,e], Ling Fang [a], Kathrin Naegeli [f,g], Andrés Rivera [h], Sebastián Cisternas [c], Tatjana Münster [a], Margit Schwikowski [a,e]

[a] Laboratory of Environmental Chemistry, Paul Scherrer Institute, Villigen, Switzerland
[b] Institute of Earth Observation, EURAC research, Bolzano, Italy
[c] Glaciologia y Cambio Climatico, Centro de Estudios Cientificos (CECs), Valdivia, Chile
[d] Department of Geosciences, University of Fribourg, Fribourg, Switzerland
[e] Oeschger Centre for Climate Change Research, University of Bern, Bern, Switzerland
[f] Department of Geography, Remote Sensing Laboratories, University of Zurich, Zurich, Switzerland
[g] Institute of Geography and Oeschger Centre for Climate Change Research, University of Bern, Bern, Switzerland
[h] Departamento de Geografia, Universidad de Chile, Santiago, Chile

HIGHLIGHTS

- Combining across-scale light-absorbing impurity analysis with melt modeling
- Chemical and mineralogical properties show mobilized particles from mine deposits.
- Light-absorbing impurities contribute to elevated mass loss of Olivares glaciers.
- Mass balance is sensitive to ice albedo changes.
- Accelerated seasonal snow albedo might be responsible for above-average mass loss.

GRAPHICAL ABSTRACT

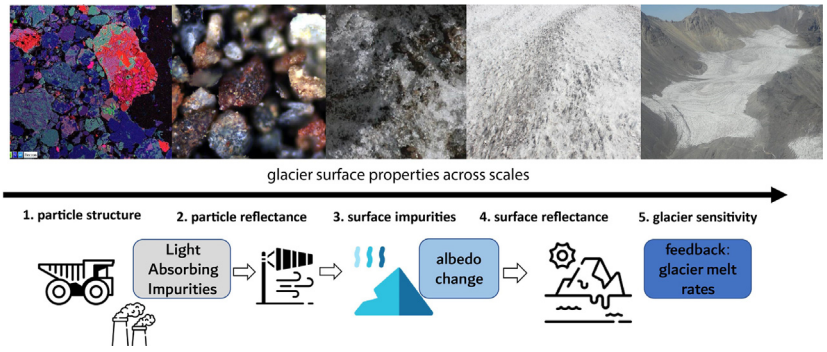

ARTICLE INFO

Editor: José Virgílio Cruz

Keywords:
Light-absorbing impurities
Glacier albedo across scales
Glacier mass balance sensitivity
Mining activities

ABSTRACT

We have investigated the source and role of light-absorbing impurities (LAIs) deposited on the glaciers of the Olivares catchment, in Central Chile. LAIs can considerably darken (lowered albedo) the glacier surface, enhancing their melt. We combined chemical and mineralogical laboratory analyses of surface and ice core samples with field-based spectral reflectance measurements to investigate the nature and properties of such LAIs. Using remote sensing-based albedo maps, we upscaled local information to glacier-wide coverage. We then used a model to evaluate the sensitivity of surface mass balance to a change in ice and snow albedo. The across-scale surface observations in combination with ice core analysis revealed a history of over half a century of LAIs deposition. We found traces of mining residuals in glacier surface samples. The glaciers with highest mass loss in the catchment present enhanced concentrations of surface dust particles with low reflectance properties. Our results indicate that dust particles with strong light-absorbing capacity have been mobilized from mine tailings and deposited on the nearby glacier surfaces. Large-scale assessment from satellite-based observations revealed darkening (ice albedo lowering) at most investigated glacier tongues from 1989 to 2018. Glacier melt is sensitive to ice albedo. We believe that an accelerated winter and spring snow albedo decrease, partially triggered by surface impurities, might be responsible for the above-average mass loss encountered in this catchment.

* Corresponding author at: Laboratory of Environmental Chemistry, Paul Scherrer Institute, Villigen, Switzerland.
E-mail address: martina.barandun@eurac.edu (M. Barandun).

http://dx.doi.org/10.1016/j.scitotenv.2022.155068
Received 1 November 2021; Received in revised form 29 March 2022; Accepted 2 April 2022
Available online 9 April 2022

1. Introduction

Impurities on snow and glacier surfaces consist typically of aerosols, rock fragments from the surrounding valley walls, glacial deposits, and/or organic matter (e.g. Naegeli et al., 2015; Cook et al., 2016; Dal Farra et al., 2018; Barraza et al., 2021). Light-absorbing impurities (LAIs) are materials that present high absorption in the visible range of the solar spectrum (390–700 nm, Dal Farra et al., 2018). LAIs are typically grouped into black carbon (BC), organic matter, and mineral dust (Warren, 1980), and can considerably reduce snow and ice albedo (Takeuchi et al., 2001). BC refers to the strongly light-absorbing component of soot and is emitted both naturally and anthropogenically by incomplete combustion of fossil fuels and biomass burning. Organic matter, such as humic substances, can be transported or produced in situ through biogenic processes. The highest accumulations of organic matter are found in cryoconite holes on glacier surfaces (Cook et al., 2016). Cryoconites substantially reduce glacier surface albedo (Takeuchi et al., 2001). Mineral dust particles present a wide range of different reflectance properties (Dal Farra et al., 2018). The main sources of mineral dust are arid regions with low vegetation cover where fine-grained material is available and mobilized (Di Mauro et al., 2015). Mineral dust production and deposition has increased over time in many regions (Di Mauro et al., 2015).

The strongest driver for ablation on alpine glaciers is net shortwave radiation (e.g. Brock et al., 2000; Klok and Oerlemans, 2004; Pellicciotti et al., 2008; Ayala et al., 2016; Schaefer et al., 2020), and the amount of solar radiation that is absorbed at the glacier surface depends strongly on the surface albedo. Thus, glacier surface albedo determines a large amount of the energy available for snow and ice melt throughout the year. The glacier surface presents low albedo values in the ablation zone, where ice is exposed at surface over most of the summer season (e.g. Paul et al., 2008). The longer this surface is exposed, the more solar radiation will be absorbed. Rising air temperatures prolong the melting season, reduce the extent of the snow cover, and lead to shorter winter seasons. Consequently, the dark ablation surface is exposed longer to the atmosphere. This causes a positive feedback, enhancing surface melt significantly (Oerlemans and Hoogendoorn, 1989; van der Wal et al., 1992; Paul et al., 2007; Naegeli et al., 2019). Due to the increase in absorption of solar radiation by the deposited absorptive impurities, the feedback is further enhanced and can thus impact significantly on the energy balance at the glacier surface (Box et al., 2012; Brun et al., 2015; Tedesco et al., 2016). Fresh snowfall reflects a large part of the incoming solar radiation, covers the dark ice surface, and protects it from melt. During the ablation period, snow can, for a short period of time—until it melts again—, lower or even stop melt. In autumn, snowfall becomes more frequent and eventually controls the glacier-wide albedo. Factors that affect snow albedo reduction include snow aging, grain size, solar zenith angle, snow depth, the impurity ice/mixing state, particle morphology, liquid water, and presence of LAIs (Wiscombe and Warren, 1980; Warren, 1984; Hansen and Nazarenko, 2004).

Andean glaciers have a more negative specific mass balance (0.7 m w.e. yr^{-1}) for the past two decades than glaciers in most other regions worldwide (Dussaillant et al., 2019; Braun et al., 2019; Zemp et al., 2019). Main drivers for this enhanced mass loss are ongoing atmospheric warming and decreasing precipitation trends (Falvey and Garreaud, 2009; Garreaud et al., 2017). Glacier mass loss in the Andes is an important contributor to sea level rise (≈3 mm sea-level equivalent from 1961 to 2016) (Zemp et al., 2019) and represents an essential water resource for the region: snow and ice melt can contribute by up to 50% to the total annual river runoff (Huss et al., 2017). Huss and Hock (2018) modeled an up to 30% reduction in glacier melt water release into the rivers of the Central Andes in the next 100 years under an emission scenario RCP4.5 (Representative Concentration Pathways 4.5).

An acceleration of glacier mass loss for the Maipo River basin in Central Chile since 2010 has been highlighted (Farías-Barahona et al., 2020; Dussaillant et al., 2019; Hugonnet et al., 2021), partly related to the ongoing mega drought event (Ayala et al., 2020; Garreaud et al., 2020). Long-term in situ mass balance observations at Echaurren Norte Glacier underlined this trend, showing enhanced mass loss since 2009 (WGMS, 2021; Farías-Barahona et al., 2019; Masiokas et al., 2016). The Olivares catchment, a subcatchment within the Maipo River basin (Fig. 2), presents a more than twice as high glacier mass loss rate since the mid 1950s (0.29 ± 0.1 m w.e. yr^{-1}) compared with the glaciers in the surrounding subcatchments (Farías-Barahona et al., 2019). Dussaillant et al. (2019) reported a similar accelerated mass loss within the catchment from 2000 to 2018 and encountered exceptionally negative mass balance rates for the glaciers Olivares Alfa (0.85 ± 0.1 m w.e. yr^{-1}) and Paloma Norte (0.97 ± 0.1 m w.e. yr^{-1}).

To date, this above-average glacier mass loss remains unexplained. Causal links have been suggested between the role of dust particles from mining activity and dramatic mass loss of glaciers, in particular for Olivares Alfa and Paloma Norte (Cereceda-Balic et al., 2014; Malmros et al., 2016; Farías-Barahona et al., 2020; Ayala et al., 2020), although clear evidence is still lacking (Shaw et al., 2021). Cereceda-Balic et al. (2020) found substantially higher BC concentrations in the atmosphere and in snow samples from Olivares Alfa in comparison with the more southern located Bello glacier (Colorado catchment). Both glaciers are situated at ≈60 km distance to the capital city Santiago (Cereceda-Balic et al., 2020), which represents a major source of atmospheric pollution too, such as for urban BC (Huneeus et al., 2021; Lapere et al., 2021). Alfonso et al. (2019) and Rowe et al. (2019) showed increased concentrations of anthropogenic LAIs in snow samples for different sites in Central Chile. The authors highlighted elevated concentrations not only of BC but also of mineral dust, that has significant effects on snow reflectance properties.

The source and role of LAI deposition on ice and snow albedo and its associated effect on the magnitude of ablation for the Olivares catchment are not well understood. This study aims at (1) characterizing the origin and composition of LAIs detected in snow and ice, (2) quantifying the surface albedo and its spatiotemporal variability based on *in situ* measurements and satellite imagery, and (3) analyzing the sensitivity of ablation processes to snow and ice albedo changes for the glaciers located in the Olivares catchment using numerical modeling.

2. Study site

2.1. Climate and local meteorological conditions

The Olivares catchment is part of the Maipo River basin and is located in the semiarid Andes Cordillera of Central Chile about 50 km Northeast of Santiago (Fig. 1). This is one of the most glaciated areas (111 km^2 in 1955) of the Maipo River basin (Ayala et al., 2020). In the present study, we focus on the glaciers Olivares Alfa, Olivares Beta, Paloma Norte, and Juncal Sur (Table 1) but also show results for Barroso IV and Cerro Negro glaciers (Fig. 2).

Atmospheric conditions over the Olivares catchment are determined by the interaction of the Andes with large-scale circulation patterns. This catchment is under the influence of the southeast Pacific anticyclone all year around, centered at 30°S (Garreaud et al., 2013), but several synoptic mechanisms (e.g., cold fronts), including those transporting water vapor from low latitudes as atmospheric rivers, cause midlatitude storms and precipitation events over the catchment. Observed total annual precipitation over the western Andes between 32°S and 34°S ranges from 300 mm to 900 mm, depending on the location and elevation of the meteorological station (Viale et al., 2019). Over 75% of the total annual precipitation over this region occurs between April and September due to the passage of cold fronts (Viale et al., 2019). Summer precipitation due to predominant convective events also occurs but only represents around 10% of the total annual precipitation (Viale and Garreaud, 2014). Most precipitation in the Olivares catchment falls as snow (Mardones and Garreaud, 2020). Interannual variability depends on global-scale atmospheric–oceanic circulation patterns such as El Niño Southern Oscillation (ENSO), Madden–Julian Oscillation (MJO), or the Interdecadal Pacific Oscillation (IPO), among others (Garreaud, 2009; Garreaud et al., 2009). During the warm phase of ENSO (El Niño), positive anomalies in precipitation tend to occur, while during

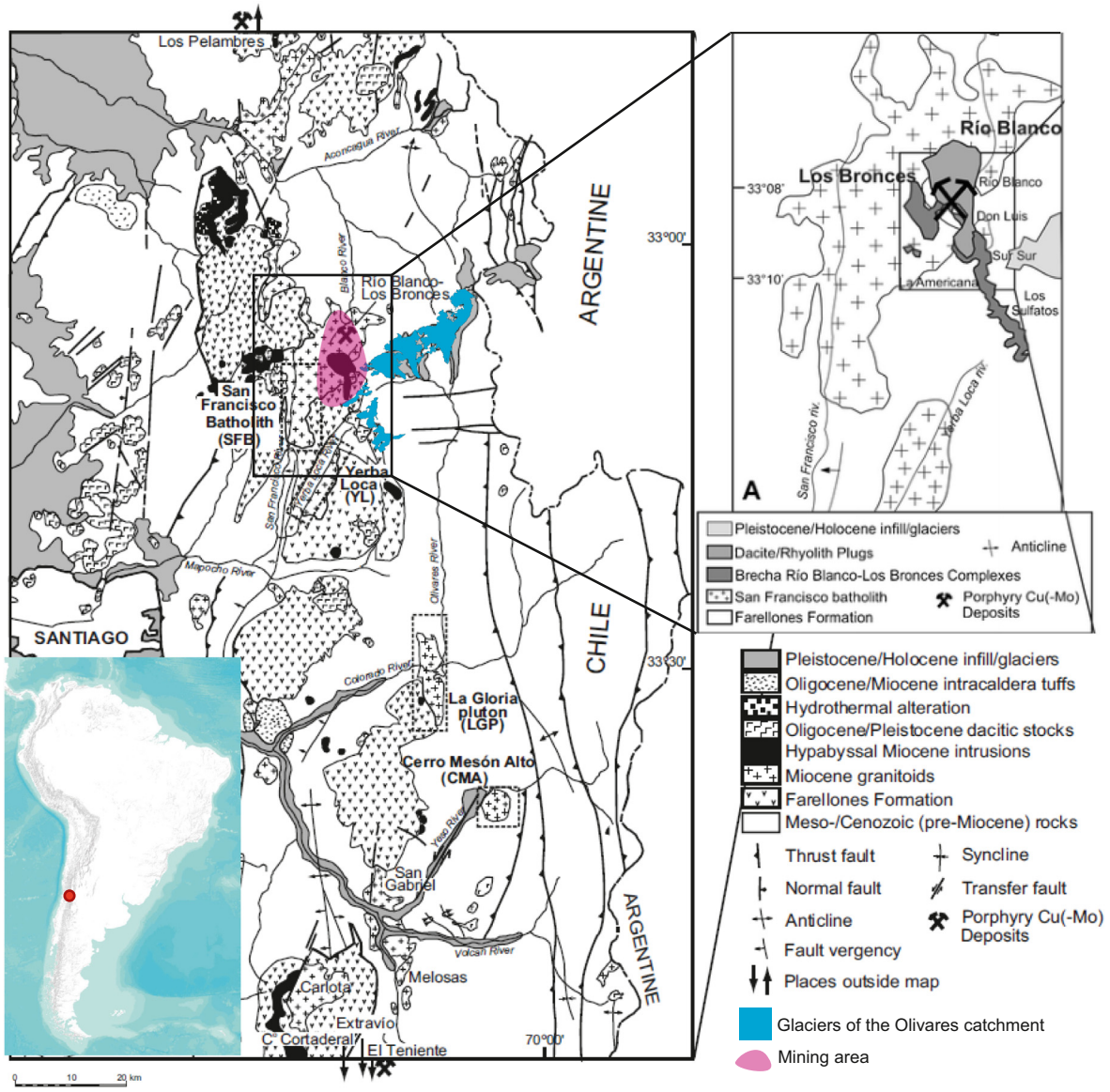

Fig. 1. Overview of the geology of the study region. Glaciers of the Olivares catchment highlighted in blue and approximate mining area in red. Inset A showing simplified geological map of the San Francisco batholith intruded into the Farellones formation (preintrusive volcanic suite) and the Río Blanco-Los Bronces breccia complexes with postmineralization dacite/rhyolite plugs. Río Blanco, Don Luís, Sur Sur, La Americana, and Los Sulfatos sectors host important Cu(-Mo) mineralization. See Appendix A.1.1 for more details. Modified from Deckart et al. (2005, 2013).

cold ENSO (La Niña), below-average precipitation is generally recorded (Masiokas et al., 2020). However, since the mega drought, negative anomalies occurred also during la Niña, El Niño, and neutral ENSO phases (Garreaud et al., 2017). The interannual variability of precipitation has been accompanied by an overall trend of precipitation decrease (e.g. Boisier et al., 2018) and a significant temperature increase in the region between 1979 and 2015 (e.g. Burger et al., 2018). Furthermore, the Andes between 30°S and 38°S have been affected by an extensive dryness since 2010, the so-called mega drought (Garreaud et al., 2017, 2020). During the mega drought, mean annual air temperature increased up to ≈0.8 °C and annual precipitation decreased up to a 50% compared with the 1986–2009 period at some locations (Shaw et al., 2021). Reduction of annual precipitation and vegetation health led to land cover degradation, exposing soil to erosion. This might have intensified the amount and transportation of airborne dust particles (e.g. Shepherd et al., 2016; Al Ameri et al., 2019).

Table 1
Topomorphological characteristics of investigated glaciers based on RGIv6.0 (RGI, 2017).

Glacier	Mean elevation (m asl)	Max elevation (m asl)	Min elevation (m asl)	Mean slope (°)	Area (km^2)
Juncal Sur	4450	5745	3826	18.1	21.04
Olivares Beta	4463	4924	3894	15.2	7.44
Olivares Alfa	4574	5037	4259	13.8	3.2
Paloma Norte	4614	4794	4452	9.5	0.6

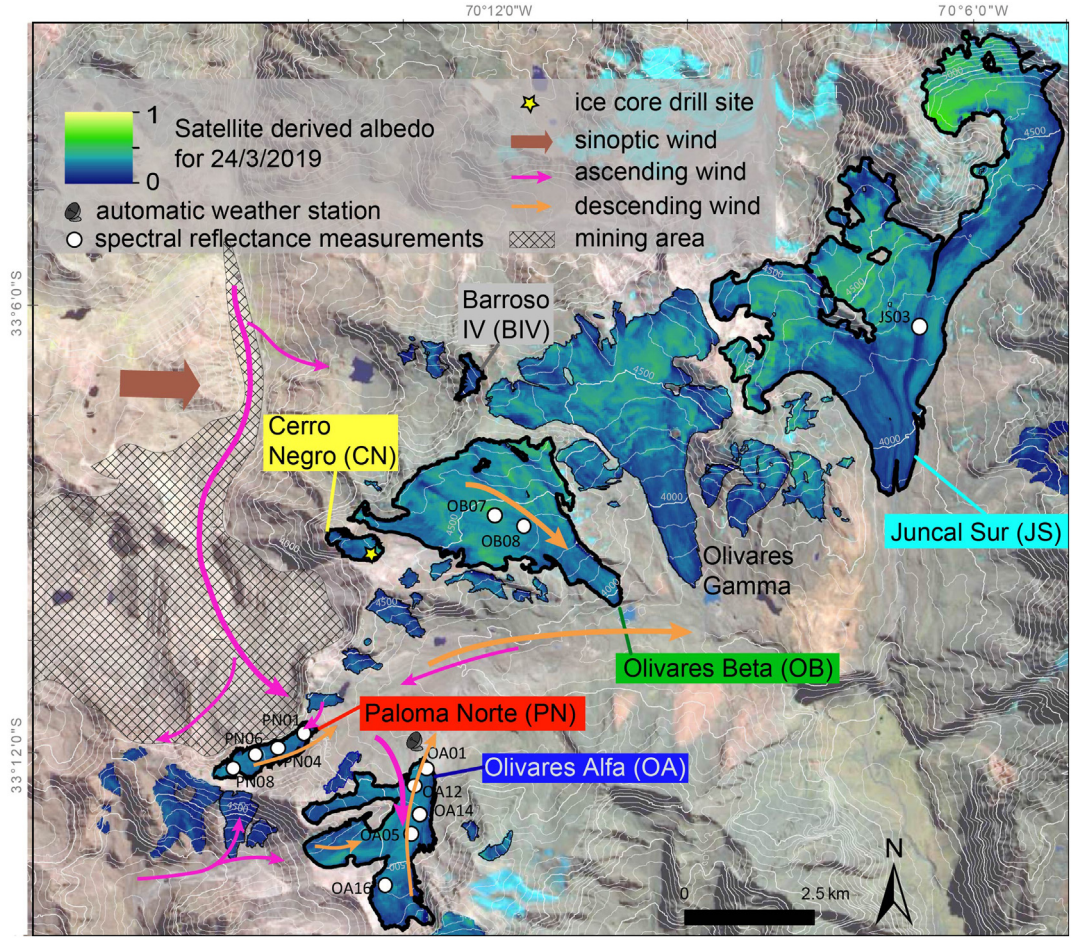

Fig. 2. Overview of the Olivares catchment on a almost snow free Landsat satellite end-of-summer image. Colored names highlighting glaciers focused in this study. Color shading within perimeters showing albedo information. White dots indicating location of field spectrometer measurements. Yellow star indicating drill location. Colored arrows indicating wind direction according to Codelco Chile (2019). Dashed area indicating approximated area directly affected by mining activity.

2.2. Geology and mining activities

First mining activities in this region date back to 1864 (Brenning, 2008; Brenning and Azócar, 2010). Today, two large copper mines are operated next to the Olivares catchment: Los Bronces and Andina (Río Blanco) mines. These mines are located northwest of the Olivares catchment area at the southeastern corner of the San Francisco batholith (Fig. 1). Explosive pressure release related to hydrothermal activity led to the formation of tourmaline-specularite (hematite)-sulfide-bearing breccia pipes (Deckart et al., 2013). Andina and Los Bronces mines are located in the breccia pipes area (Dold and Fontboté, 2001). More details on the geology and mining history of the area are provided in Appendix A.1.1. The glaciers Paloma Norte, Cerro Negro, and Olivares Beta, including the bounding ridges, are free of breccia pipe outcrops (Fig. 1).

Mineralization in the breccias contains pyrite, the chalcopyrite, bornite, and molybdenite. Large volumes of the breccias contain >3 wt% pyrite and >4 wt% chalcopyrite. In contact with surface water in a natural environment, pyrite oxidizes directly to ironoxyhydroxides. In the mine waste deposits (oxidation zone of sulfidic mine tailings), the oxidation of pyrite in contact with water leads to the formation of sulfuric acid and the lowering of the pH. This low pH leads to the precipitation of minerals such as the alkali iron hydroxy sulfate jarosite $KFe_2(SO_4)_2(OH)_6$ (pH: less3) or iron oxohydroxy sulfate schwertmannite $Fe_8O_8(OH)_6(SO)_4 \cdot nH_2O$ (pH: 3–6). Dold (2003) found both minerals in the oxidized upper layer of the tailings of the Piquenes impoundment, where the pH is low enough for their formation (pH: 2.1 — 3.5). Jarosite survives only in arid environments while, under more humid conditions and at higher pH, decomposes to ironoxyhydroxides and a sulfate phase such as gypsum (Madden et al., 2004). If jarosite reaches the surface, the only way for it to survive is to be immediately protected from liquid water (e.g., by burying it very rapidly under snow which falls periodically in the accumulation area). Jarosite cannot form under natural conditions on the glacier surface in the Olivares catchment.

3. Data and sampling

3.1. Remote sensing datasets: coarse scale

We used the glacier outline from 2020 based on PlanetScope data provided in Shaw et al. (2020) and added the outline of Paloma Norte manually delineated from a Sentinel-2 scene of 2020. We downloaded 856 scenes of the Landsat Surface Reflectance Level-2 science product (cloud cover less than 50% and spatial resolution of 30 m) for the Olivares Catchment (Landsat 4–5 TM, Landsat 7 ETM+, and Landsat 8 OLI) covering the period 1986–2019. The scenes used for glacier-wide albedo maps consist of six (TM/ETM+) or seven (OLI) individual spectral bands in a wavelength range of around 440 nm to 2300 nm (Masek et al., 2006; Vermote et al., 2016). We used the freely available void-filled Shuttle Radar Topography Mission (SRTM, Jarvis et al., 2008) digital elevation model (DEM) as topographic input.

3.2. Field sampling and measurements: local scale

In February 2019, we visually identified the following dominant glacier surface types: water, cryoconites, bright ice, dirty ice, and ice with few debris. Before taking surface ice samples (Section 3.3), we conducted field-based surface reflectance measurements (Fig. 3F) of each surface type at each sampling location spread over the different glaciers (12 sites) in a field of 20 × 20 cm (Figs. 2 and 3). At each sampling location, we also measured the reflectance spectra of a field of 4 × 4 m. Sample locations were selected to represent the entire ablation area and various elevation bands of the glaciers.

3.3. Data collected for laboratory analysis: particle to microscopic scale

In February 2019, we took 65 ice surface samples to investigate the chemical and mineralogical composition of LAIs. We sampled all visually identified glacier surface types (3–5 samples per site, Fig. 3) at 10 sample locations on Olivares Alfa, at 3 locations on Olivares Beta, at 4 locations on Paloma Norte, and at 1 location on Cerro Negro, Barroso IV, and Juncal Sur, each. All dominant surface types were sampled for each location when present (Fig. 3A–F). We collected a surface sample of each surface type for which a reflectance spectra was recorded. Sample area was typically 20 × 20 cm large and 1–2 cm deep (Fig. 3G). Larger rock fragments (not wind transported) were sampled from Olivares Alfa, Paloma Norte, and Olivares Beta.

A 7.43 m-long ice core was collected on Cerro Negro (Chile, 33°08′37.5″ S, 70°13′38.5″ W, 4604 m asl, Fig. 2) on April 30, 2017. This location was part of the accumulation area (surface heightening) in the past, but in recent years, the equilibrium line moved above the ice core drill site. This resulted in the recently observed surface lowering.

3.4. Data used for numerical modeling: across scales

To run a mass balance model, climate data were obtained from ERA5-Land reanalysis (Muñoz-Sabater et al., 2021). Hourly air temperature and incoming shortwave radiation recordings were downloaded between the years 1990 and 2020. The mass balance model, however, runs with a daily time step. To determine air temperature at the elevation of each glacier pixel, we used air temperature lapse rates derived from the closest weather stations (for location see Fig. 2) managed by the Direccion General de Aguas (DGA). These weather stations were Valle Olivares and Glaciar Olivares Gamma, located at 2840 m asl and 3600 m asl, respectively, below the limit of the glaciated area of the catchment. The obtained mean air temperature lapse rate was $-8.4\ ^{\circ}C\ km^{-1}$. We used Landsat-based albedo maps (Section 4.1.1) for distributed ice albedo model input and for snow albedo aging estimates during the winter season.

4. Methods

An overview of the workflow is shown in Fig. Appendix A.1.

4.1. Remote sensing observations: coarse scale

4.1.1. Glacier albedo change

We derived spatially distributed shortwave broadband albedo maps from Landsat satellite imagery (TM, ETM+, OLI) for all available scenes from 1986 to 2019 based on Naegeli et al. (2019). After cloud filtering and masking out Scan Line Correction (SLC)-off void-stripes (Naegeli et al., 2019), we applied the narrow-to-broadband conversion by Liang (2001) to obtain shortwave broadband albedo from the individual spectral bands. We separated snow-covered from ice pixels following Barandun et al. (2021) and Naegeli et al. (2019). This surface classification is based on the surface albedo of snow and ice over the glacier area and takes into account their spatial distribution. Due to the limited availability of suitable images prior to 1989, we calculated the trends from 1989 to 2018. For this period, one end-of-summer Landsat snapshot was collected manually for each of the 29 years. We did not find suitable images for 1992 or 1998. We set the minimum number of scenes necessary to calculate the albedo trend of one individual grid cell to 50% (14 scenes) of the maximal available scenes. We used a nonparametric Mann–Kendall test (Mann, 1945; Kendall, 1948) to evaluate the confidence level of the trends (significant at the 99%, 95%, 80% level or not significant).

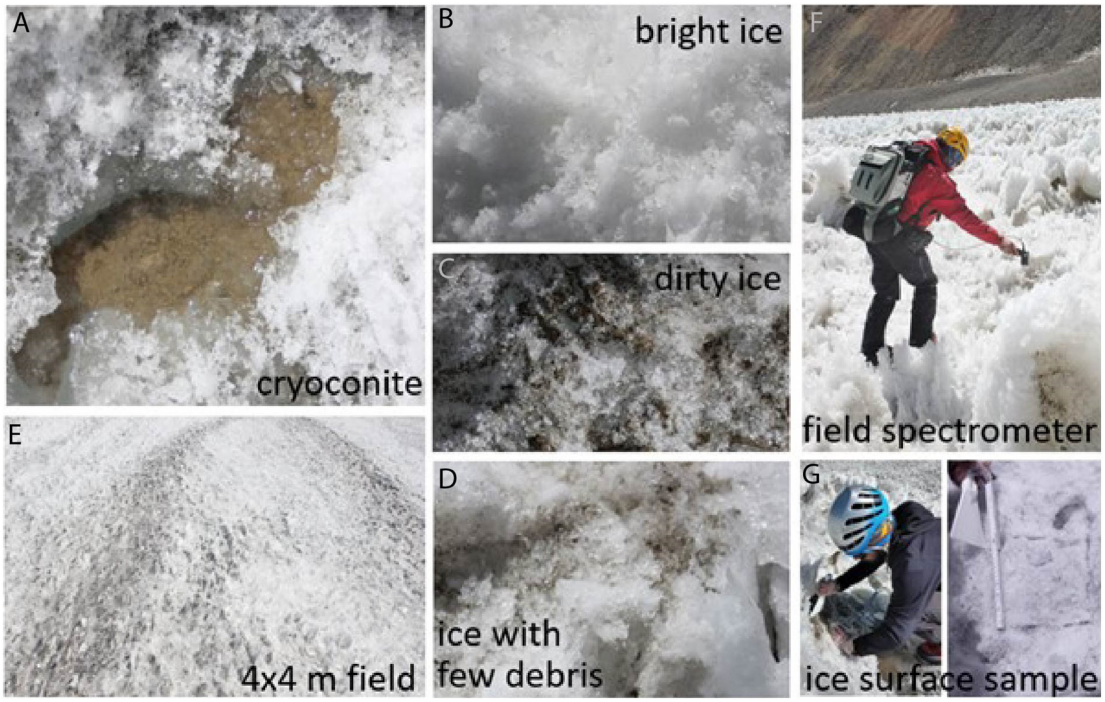

Fig. 3. A.–D. Images of measured and sampled surface types encountered on the glacier surface in Olivares catchment and E. of representative 4 by 4 m area of a sampling site with all possible surface types; example of F. In situ Fieldspec spectral reflectance measurements in Penitentes field and G. surface ice sampling.

Subseasonal glacier-wide albedo variations and winter snow albedo changes were investigated taking advantage of the higher frequency of high-quality Landsat 8 scenes available since 2013.

4.2. Field measurements: local scale

4.2.1. In situ reflectance measurements

We used a field spectrometer [analysis spectral device (ASD); FieldSpec Pro, Boulder, USA] to measure nadir in situ radiometrical properties of the different surface types. We measured a spectral range of 350–2500 nm. The FieldSpec measurements were taken under clear-sky conditions around noon between February 28, 2019 and March 3, 2019, prior to the surface sampling. The measurements procedure follows Naegeli et al. (2015), and the sites correspond to (1) the same exact location at which each visually identified surface type was sampled (field of measure 20 by 20 cm) and (2) a representative field of 4 by 4 m of the sampling site, containing all identified surface types present at the location (Fig. 3E & F).

4.3. Laboratory analysis: particle to microscopic scale

4.3.1. Organic and elemental carbon analysis

Concentrations of organic carbon (OC) and elemental carbon (EC) were determined with a thermooptical OC-EC analyzer (Sunset Laboratory Inc., USA) using the Swiss_4S protocol for OC–EC separation (Zhang et al., 2012). Only water-insoluble OC (WIOC) can be detected using this method; we assumed the soluble part to be negligible. EC and BC are both reflecting concentrations of soot but differently denoted due to the difference in the analytical technique applied (Lavanchy et al., 1999). The surface ice samples were melted at room temperature; OC and EC were extracted by filtration and then combusted. The analysis was conducted for a sample of each visually identified surface type (Fig. 3) and with a minimum available particle material of 2.7 and 4.0 mg. Number of samples per glacier is presented in Supplementary Table A.4. Mineral dust concentration was determined subtracting the amount of organic matter (1.9 times OC, El-Zanan et al., 2005) and EC from the sample initial weight, assuming the noncombusted fraction to be composed purely of minerals. We calculated the amount of LAIs and water in g m^{-2} for each sample.

Radiocarbon (^{14}C) analysis was performed on the OC and EC samples with a 200 kV compact accelerator mass spectrometer (AMS; MIni CArbon Dating System, MICADAS) at the Laboratory for the Analysis of Radiocarbon with AMS (LARA) based in the University of Bern. For source apportionment, the obtained $F^{14}C$ was converted to the fraction of nonfossil (f_{NF}) using the following equation:

$$f_{NF} = F^{14}C / f_{NF}(REF) \quad (1)$$

Fossil carbon is characterized by $F^{14}C = 0$ due to the decay of ^{14}C with a half-life of 5730 years. The $F^{14}C$ value of contemporary carbon from biogenic sources and biomass burning $f_{NF}(REF)$ was estimated using a tree-growth model. Details of the analytical methods are provided in Appendix A.2.1. Based on mass balance, the fractions contributing to OC and EC from fossil and nonfossil sources, respectively, were calculated for all our samples (Supplementary Table A.4).

4.3.2. Trace element concentration in surface samples

We analyzed trace element concentrations in the surface ice samples with inductively coupled plasma optical emission spectrometry (ICP-OES; VISTA AX, Agilent Technologies, Inc., USA) and performed a full digestion. Number of samples is presented in Supplementary Table A.4. The samples were melted and dried in a clean bench, put in a wolfram carbide grinding jar, and then homogenized with a vibrating mill [MM200 (Retsch)]. Per sample, 50 mg of the homogenized material was added into a 15 ml-pp tube and acidified with HNO_3/HF/HCl. The solution was mixed using a vortex mixer and let to react during 30 min at ≈95 °C. The HF was masked with 5% boric acid. The end volume of each sample of the total digestion was 10 ml. Not all material of the samples could be dissolved, but the high-resolved fine precipitates were mixed before aliquot withdrawal. These were then diluted from 1/10 to 1/1000. External calibration with a dilution series from a stock solution of a multielement standard [calibration range 0 (blank) - 2 ppm] was used.

For all samples, enrichment factors *EF* above the natural background were calculated for each trace element *M* following Tapia et al. (2018) to identify possible anthropogenic pollution through external sources as follows:

$$EF = \frac{M_{sample}/R_{sample}}{M_{background}/R_{background}} \quad (2)$$

We used background values provided by Oliveros et al. (2007) for northern Chile and *Al* as reference element *R*. *EFs* below 1 indicate natural occurrence; *EFs* between 1 and 10, possible natural and anthropogenic contribution; and *EFs* higher than 10, clear anthropogenic pollution.

4.3.3. Ice core - chemical analysis and dating

For the analysis of trace elements (TE), BC, and major ions, individual samples were cut from the inner uncontaminated part of the core under clean conditions in the cold room at −20 °C using a stainless-steel band saw with a Teflon coated saw guide and table surface. The continuous sampling was performed with a resolution of 5 cm, and samples (≈15 ml each) were stored frozen in precleaned 50 ml polypropylene vials, awaiting analysis. A lower, but still continuous, sampling resolution of around 40 cm was applied for the larger volume ^{210}Pb samples (around 200 ml), which were stored frozen in clean PETG containers. Details of the analytical methods are provided in Appendix A.2.2. Concentrations of trace elements in the ice core were analyzed using inductively coupled plasma sector field mass spectrometry (ICP-SF-MS; Element 2, Thermo Fisher Scientific, Germany, details in Appendix A.2.2). For a full method description, also see Eichler et al. (2017) and Avak et al. (2018). Concentrations of BC - hereinafter referred to as refractory black carbon (rBC) according to the laser-based incandescence method used - were determined with a Single Particle Soot Photometer (SP2, Droplet Measurement Technologies, Inc., Boulder, USA, Appendix A.2.2). All details can be found in Osmont et al. (2018). Concentrations of major ions were analyzed by ion chromatography (Metrohm 850 Professional IC, Methrom, Switzerland, Appendix A.2.2). ^{210}Pb activity was determined continuously throughout the core, following the method described in Gäggeler et al. (1983) and Gäggeler et al. (2020) (Appendix A.2.2). Strongly elevated concentrations were observed in the upmost 0.5 m water equivalent (w.e., depth unit converted from meter by accounting for the measured density of the ice), indicating strong enrichment of impurities at the surface accumulated over several years due to postdepositional melt-related removal of the initially deposited snow/ice matrix (Appendix A.2.3). This layer was not considered in further analyses.

Dating of the Cerro Negro ice core was obtained using a multiparameter approach, with different independent dating methods (Appendix A.2.3). We estimated the year of origin of the surface layer to ≈1956 ± 11 years.

We calculated the trends of the enrichment factors of the different elements along the annual layers of the ice core profile using a nonparametric Mann–Kendall test (Mann, 1945; Kendall, 1948) to evaluate the confidence level of the trends (significant at the 95%, 90%, 80% level or not significant).

4.3.4. Bulk mineralogical composition

To obtain the quantitative mineralogical composition of the deposit, large debris particles (not wind transported) at Olivares Alfa, Paloma Norte, and Olivares Beta were powdered and analyzed with a Rigaku Ultima IV diffractometer equipped with a position sensitive detector. Diffractograms were recorded between 5 °C and 70 °C in step-scan mode (0.02 °C/step and 1 min/°C). The CuKα radiation was filtered with a nickel foil. Quantitative phase analysis by Rietveld refinement (Bish and Post, 1993) was performed on the recorded patterns using the PDXL2 software package (Taylor, 1991). The refined instrumental parameters are the zero shift, the sample displacement, and the peak shape, modeled with a

pseudo-Voigt profile function. The structure parameters for the phases present in the sample were taken from the ICDD data base. The sample parameters, which were refined, were the unit cell parameters, the isotropic overall temperature factor, the fraction of each phase present (through the scale factor), and for the phyllosilicates as well as albite, the preferred orientation parameters using the March-Dollase formalism. The atomic positions and the site occupancies were kept fixed during the refinement. Iterations were performed until the refinement converged.

4.3.5. Hyperspectral imaging microscopy

We determined the reflectance spectra of LAIs in the ice samples using a hyperspectral imaging microscope (HIMS, CytoViva, Inc.). This method was developed by Dal Farra et al. (2018) and enables to capture the hemispherical directional reflectance of each class of LAI in a heterogeneous sample. HIMS allows the identification of the impurities and the characterization of their reflectance. Spectra were collected between 400 and 1000 nm with a 2.5 nm spectral resolution (Beach et al., 2015) and a spectral sampling interval of 1.2 nm. At 100× magnification, the pixel in the hyperspectral image corresponds to ≈129 nm × 129 nm. Number of samples is presented in Supplementary Table A.4. In addition to the surface samples, three samples from the ice core at Cerro Negro were analyzed. The sampling procedure follows Dal Farra et al. (2018).

4.3.6. Scanning electron microscopy

After HIMS measurement, the particles were covered with a 50-nm carbon layer to enhance electric conductivity and then imaged using scanning electron microscopy (SEM; FEI Sirion FEG). Energy dispersive spectroscopy (EDS; Oxford Aztec) was used to obtain chemical maps. EDS spectra and maps of dust samples from Olivares Alfa, Beta, Paloma Norte, Juncal Sur, Cerro Negro, and Barroso IV were obtained. We also analyzed the surface and ice core samples from Cerro Negro (same sample number as measured for HIMS; Supplementary Table A.4). To eliminate the effect of topography and to obtain quantitative EDS analyses, polished sections of the particles and fragments were prepared. Element concentrations and stoichiometry of pure phases were obtained from the PAP (Pouchou and Pichoir, 1991) corrected intensities extracted from the spectra. With the high-resolved element maps obtained from the polished sections, we were able to distinguish less-abundant mineral phases. Mapping locations on the samples were chosen randomly. Different grains were mapped, and homogeneous analyses were quantified and normalized. Phase identification was based on the stoichiometry. Special attention was paid to iron-containing phases known to have low reflectance.

4.4. Numerical modeling: across scales

4.4.1. Surface mass balance sensitivity to albedo change

The goal of this modeling experiment is to quantify the change in melt and surface mass balance (SMB) rates under different distributed ice albedo values. Consequently, we assessed the sensitivity of mass balance to temporally variable distributed ice albedo. Landsat-based albedo maps from 1991, 1999, 2010, and 2018 provided distributed ice albedo information from nearly snow-free moments in time. We run the mass balance model with the same parameter set four times from hydrological years 1990/91 to 2019/20 and solely changed the ice albedo. We then related the resulting cumulative melt over a melt season with the average of the corresponding distributed ice albedo for each glacier and compared the relation among the four runs per glacier. Therefore, the changes in melt rates provide the sensitivity to the ice albedo used for modeling. In the present study, we do not attempt to identify the cause of high or low melt rates of individual years, but only show how melt rates changed in relation to changes in the observed ice albedo.

Accumulation was estimated using total precipitation obtained from the ERA5-Land reanalysis (Muñoz-Sabater et al., 2021) for each grid point containing the assessed glaciers. Surface accumulation was assumed to be the fraction of solid precipitation (r), according to Weidemann et al. (2018):

$$r = 0.5 \cdot (-\tanh((T_{air} - 1) \cdot 3) + 1) \quad (3)$$

The proportion of solid to total precipitation is scaled between 100% and 0% within an air temperature range of 0 °C to 2 °C. Under 0 °C, the fraction of solid precipitation is 100%, while above 2 °C, the fraction of solid precipitation is 0%. An enhanced temperature-index model based on Pellicciotti et al. (2008), integrating albedo, incoming shortwave radiation, and air temperature was used to estimate melt rate:

$$M = \begin{cases} TF \cdot T + SRF \cdot (1-\alpha) \cdot I & T_{air} > T_t \\ 0 & T_{air} \leq T_t \end{cases} \quad (4)$$

where M is melt rate (mm w.e. h^{-1}), T is air temperature (°C), α is albedo, and I is incoming shortwave radiation (W m^{-1}). TF is the temperature factor (mm d^{-1} $°C^{-1}$); SRF is the shortwave radiation factor (m^2 mm^{-1} W^{-1} h^{-1}); and T_t is the threshold temperature for melt onset. The empirical factors TF and SRF were assumed constant; due to the lack of direct observations of the glaciers studied in the present work, the values were those adopted from Ragettli et al. (2014) that used TF = 0 and SRF = 0.0105 for the nearby glacier Juncal Norte. Although the focus was to assess the differences between several ice albedo conditions, the T_t parameter was adjusted for each glacier to match the geodetic mass balance estimated by Hugonnet et al. (2021) during the period 2000/01–2018/19 in 5-year time steps. The resulting T_t values vary between 0 and 3 °C. The comparison shows that our modeled mass balance is in the range of the uncertainties given by Hugonnet et al. (2021) for the four analyzed glaciers and all periods (Fig. Appendix A.4). The root mean-square error of this comparison was 0.19 m w.e. for Olivares Alfa, 0.26 m w.e. for Paloma Norte, 0.15 m w.e. for Olivares Beta, and 0.12 m w.e. for Juncal Sur. These values were then assumed as the uncertainty of the model given by the choice of the parameters.

Fields of spatially distributed air temperature over each glacier surface using the SRTM at 90 m resolution were estimated with an observed catchment-scale mean lapse rate of −8.4 °C km^{-1}, which was obtained by comparing the DGA (Glaciar Olivares Gamma) weather station with the Valle Olivares weather station (2840 m asl) during the available common period of observations from May to November 2014. As the correction of the ERA5 air temperature was performed using off-glacier observations, a reduction of 1 °C was introduced in the distributed air temperature field to account for the cooling effect of the glacier surface over the first meters of the atmosphere, following (Ayala et al., 2016). Incoming shortwave radiation time series for each glacier were obtained from the grid point containing the glaciers and adjusted by aspect and slope using the SRTM at 90 m resolution (Fig. Appendix A.5).

Finally, spatially distributed albedo derived from largely snow-free Landsat images obtained at the end of the summer of the years 1991, 1999, 2010, and 2018 were used as input to the model. The albedo parameterization by Oerlemans and Knap (1998) was used when the glacier surface was covered by snow. This model is based on the transition of the albedo from fresh snow to firn. Results of the daily modeled albedo were compared at glacier-wide scale with those estimated using Landsat winter images for the same dates (Fig. Appendix A.6). The root-mean-square error of this comparison was around 0.06 (Juncal Sur and Olivares Beta), 0.10 (Olivares Alfa), and 0.13 (Paloma Norte). The snow albedo parameterization captures the decay of the snow albedo, but with larger uncertainties for Paloma Norte glacier. Four runs were then performed using the same meteorological data (air temperature and incoming shortwave radiation) and the same parameter set between the hydrological years 1990/91 and 2019/20. Only ice albedo information was changed. Finally, SMB was estimated using the results from the accumulation and melt quantification. A relation between albedo and melt was thereby established.

5. Results

5.1. Remote sensing observations: coarse scale

5.1.1. Spatio-temporal albedo changes

We analyzed ice and snow albedo changes, looking at each component separately, and subseasonal glacier-wide albedo change. Ice or snow albedo changes indicate the actual surface albedo change of the respective surface type snow or ice, while average glacier-wide albedo contains a mixed signal of surface albedo change of the individual surface type and of a changing surface type (from snow to ice and vice-versa). Average glacier-wide albedo can thus be used as a proxy for the glacier mass balance (Brun et al., 2015).

The negative temporal ice albedo trends from 1989 to 2018 indicated the strongest darkening of the surface area in the ablation area of Juncal Sur, followed by changes at the glacier tongues at Olivares Alfa and Beta (Fig. 4). Pixels with a significant positive trend were found on all glaciers, in particular on Paloma Norte. Affected pixels were located generally above the median glacier elevation and in rather flat terrain (Fig. 2).

Snow albedo calculated from a satellite scene at the end of winter, when the entire glacier area was still snow covered (November 9, 2014, Fig. 5), was ≈0.6 for all glaciers except for Paloma Norte, whose surface snow albedo was 0.49. Snow albedo changes during the winter season of 2014–2016 and 2018 observed on Landsat 8 images clearly highlight the accelerated decrease at both Paloma Norte and Olivares Alfa (Fig. 5). While at Juncal Sur and Olivares Beta, snow albedo stayed relatively constant throughout the entire investigated winter seasons, at Paloma Norte and Olivares Alfa, the snow albedo decrease already started in late July, early August.

We investigated average glacier-wide albedo (including both snow and ice areas) from 2014 to 2018 on images of the Landsat 8 sensor. Average glacier-wide albedo is lowest at the end of the summer, when ice is exposed at the surface, indicating a high snowline position. Glacier-wide albedo at the end of the summer is similar for most years and glaciers investigated (Fig. 6). Olivares Alfa and Paloma Norte show higher winter glacier-wide albedo than Juncal Sur and Olivares Beta and reach peak albedo faster. This is because the glacier tongues of Juncal Sur and Olivares Beta reach further into the valley and take more time to be entirely snow covered, keeping the glacier-wide average albedo lower at the beginning of the winter season. Although, these glaciers, due to their size, take longer to be entirely snow free at the end of the winter season, exhibit lower mean glacier-wide albedo due to an earlier snow melt onset at lower elevations. Compared with Olivares Beta and Juncal Sur (located further away from the

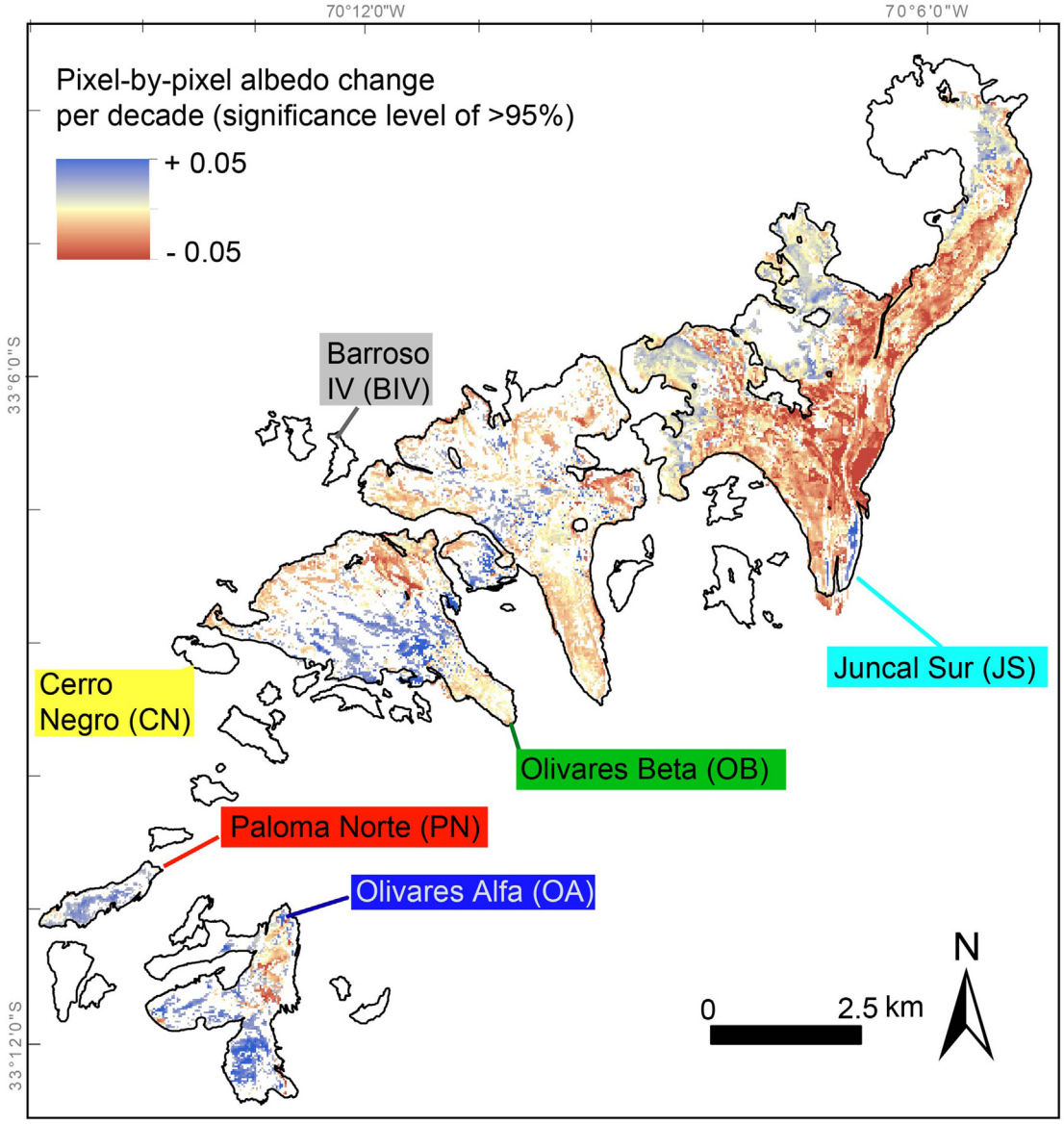

Fig. 4. Ice albedo trend of each pixel with a significant trend at 95% level or higher from 1989 to 2018.

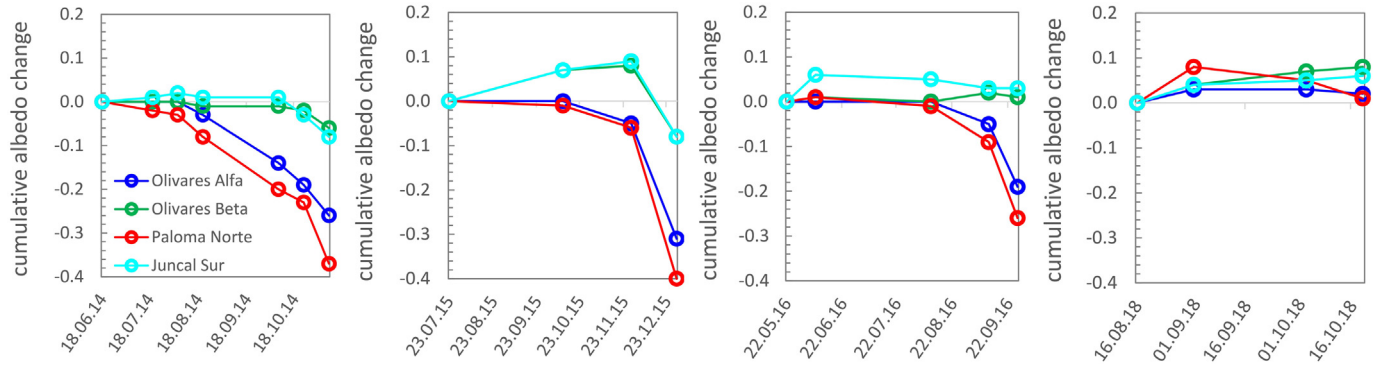

Fig. 5. Cumulative snow albedo changes for different studied glaciers during winter season (June to December) from 2014 to 2018 based on albedo maps derived from Landsat 8 surface reflectance product. Snow albedo changes summed up from one observation date to the next to calculate cumulative albedo change over the winter season. Not enough images were available for 2017.

mines), glaciar-wide albedo in Paloma Norte and Olivares Alfa (located close to the mines) starts do decrease already in midwinter, despite their higher located glacier tongues and similar mean glacier elevation (Table 1). The albedo decline continues until the end of the summer. For Olivares Beta and Juncal Sur, however, the drop starts later and the glaciers maintain a higher glacier-wide surface albedo during most of spring and early summer (Fig. 6). This can be partly explained by bigger accumulation areas in Olivares Beta and Juncal Sur, varying snowpack distribution and different snow aging and dust deposition (Wiscombe and Warren, 1980; Rowe et al., 2019).

5.2. Field measurements: local scale

We used *in situ* observations to investigate the point ice albedo for the Olivares glaciers. Differences between direct (measurement fields of 4 m by 4 m) and remote sensing derived albedo (30 m pixels) are considerable due to the inherent different nature of the measurement setup (Lucht et al., 2000; Cook et al., 2017). Therefore, we analyzed these results independently. The spectral reflectance obtained from FieldSpec measurements is highest for Paloma Norte, followed by Olivares Beta (Fig. 7). Olivares Alfa shows the lowest values. However, the spread per glacier is relatively large and depends on the share of analyzed surface types contained within the field measurement and the measurement location on the glacier (Fig. 7). Measurements at the glacier tongue (PN01, PN04, OA01, OA12, OA14, J03; Fig. 2) generally show lower reflectance.

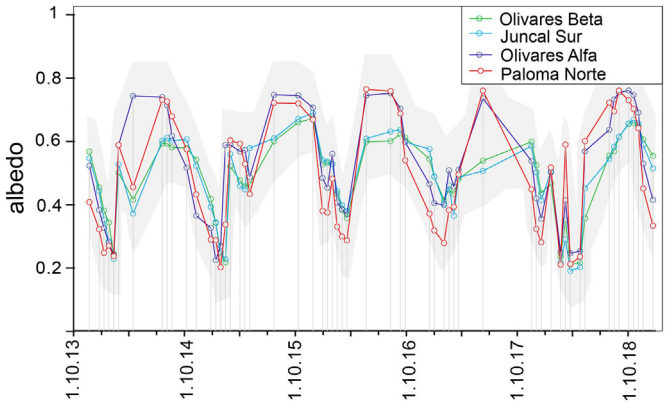

Fig. 6. Seasonal evolution of glacier-wide albedo at Olivares Alfa and Beta, Juncal Sur, and Paloma Norte from 2013 to 2018 from all available cloud-free Landsat 8 scenes. Grey lines mark all individual Landsat scenes used (n = 58). Shaded area indicates standard deviation of glacier-wide albedo (on average = ±0.13).

5.3. Laboratory analysis: particle to microscopic scale

5.3.1. Characteristics of light-absorbing impurities

The surface samples analyzed contain on average 5 wt% (STD = ±5 wt %) of LAIs and 95 wt% (STD = ±5 wt%) H_2O in the form of snow, ice, or firn melt. Average LAIs concentration in surface samples ranges between ≈90 g m^{-2} and ≈230 g m^{-2} and is similar for all studied glaciers. Concentration might be affected by wash out and surface heterogeneity and does not reflect daily deposition rates. The majority of LAIs encountered on the surface of the studied glaciers in the Olivares catchment are mineral dust particles (>99 ± 1%). Samples classified as dirty ice (Fig. 3) present a LAI concentration > 200 g m^{-2}; ice with few debris, between 50 g m^{-2} and 200 g m^{-2}; and bright ice, <50 g m^{-2}. Bright ice shows a smaller OC/EC ratio, which means higher EC content compared with OC content (Fig. 3B and Fig. Appendix A.7). On average, OC concentrations are about ten times higher than EC concentrations, but both with relatively high sample-to-sample variability. Most OC in samples from Olivares Alfa, Beta, and Paloma Norte is from nonfossil sources, while the majority of EC is of fossil origin (Fig. Appendix A.7). We found a notably high concentration of fossil EC in the samples from Paloma Norte taken in 2019 (Fig. Appendix A.7). For Juncal Sur, Barroso IV, and Cerro Negro, the number of samples is insufficient to be representative (<5).

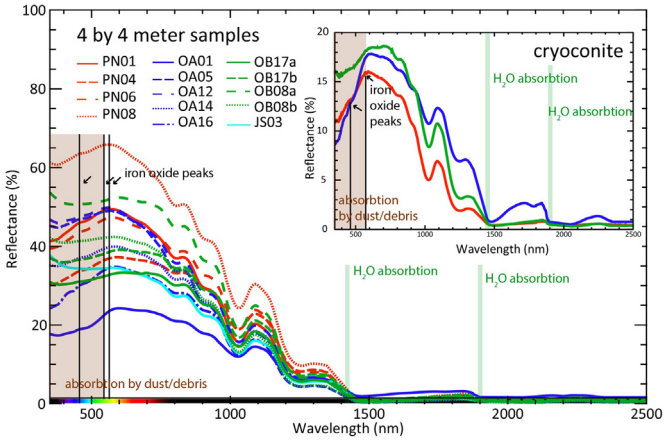

Fig. 7. Normalized spectral reflectance obtained for different measurements of fields of 4 m by 4 m and three cryoconite samples (inset) at different sampling locations of Olivares Beta, Juncal Sur, Olivares Alfa, and Paloma Norte. Brown bar indicating spectral range where effect of debris and dust absorbs most radiation. Green bars indicating absorption through organic material and liquid water. Black arrows and lines show reflectance peaks of iron-oxides (hematite/geotite; Wu et al. (2016)).

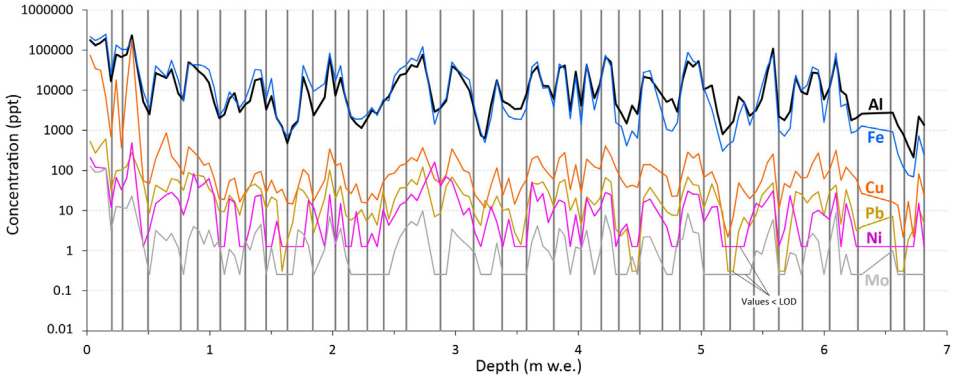

Fig. 8. Selected trace element concentration profiles from Cerro Negro ice core. Vertical grey lines indicating annual minima (meteorological winter). Values for concentrations below limit of detection replaced by value of these limits. Note logaritmic y-axis scale.

5.3.2. Enrichment of trace elements

The trace element concentration detected in the surface ice samples, containing several years of LAIs accumulation, are generally low for Juncal Sur, Barroso IV, and Olivares Beta (located further away from the mines) and high for Cerro Negro, Paloma Norte, and Olivares Alfa (located close to the mines) (Fig. Appendix A.8). Calculated enrichment factors *EFs* are higher than 10 for Cu, Mo, Pb, and S in the Cerro Negro, Paloma Norte, and Olivares Alfa samples, indicating nonnaturally high enrichment (Fig. 9). Ni and Co are strongly enriched for Olivares Alfa. Olivares Beta shows enriched Mo, Pb, and S. *EFs* for Juncal Sur and Barroso IV remain below 10 for all investigated trace elements (Fig. 9). *EFs* of other elements (Ba, Co, Fe, K, La, Zn, Zr) are between 1 and 10 for most glaciers. We renounce a detailed comparison between *EFs* of surface and *EFs* of ice core samples because LAIs in surface samples accumulated over an unknown period of time and thus were likely affected by different surface processes such as wash out, whereas samples from the ice core represent the trace element accumulation in the respective individual layer corresponding to a defined year. Surface concentrations are therefore used to allow for a general comparison between different glaciers in the catchment. Nevertheless, we found the same elements enriched in the ice core and surface samples of Cerro Negro (Fig. 9). Summarized for the annual layers (annual average concentrations) over the entire profile, Cu, Mo, and Pb are clearly enriched (*EFs* > 10) and Ni shows an average *EFs* of ≈5. *EF* between 1 and 10 were additionally found for Ba, La, Na, Fe, and Co. Along the ice core depth profile, we analyzed element concentration (Fig. 8) and evolution of enrichment of trace elements over time (Fig. 10). The deeper the section, the older the ice and the contained impurities, with the bottom of the core estimated to contain material deposited on the surface in the mid 1920s (Appendix A.2.3). The first 50 cm contain material accumulated from around 1960 to 2017 and thus represent a multilayer concentration similar to the surface samples altered by surface effects as described above. This uppermost part of the ice core was thus excluded from the trend analysis. We found a significant (at the 95% significance level) increasing trend of enrichment with time (towards surface) for the following elements: Fe and Co with *EFs* > 1 and Ni, Mo, and Pb with *EFs* > 10 (Fig. 10). *EF* of Cu did not increase significantly over time. *EF* of Fe and Co show an increasing trend ranging between *EF* = 1 and *EF* = 10; this indicates a potentially increasing anthropogenic contribution to the steady natural occurrence.

5.3.3. Mineral composition and spectral properties of dust particles

All samples, independently of their provenance, present similar bulk mineralogical composition. The main minerals are those found in metamorphic rocks with granitic composition (e.g., gneisses with quartz, albite, muscovite, chlorite). Rietveld refinement of the last three phases was difficult because of their variable compositions and polytypic stacking for the last two. The refinements closed with Rwp's of 5–10%.

In Fig. 11, all phases containing iron are highlighted in an element map of Paloma Norte (examples for other glaciers can be found in Fig. Appendix A.10 to Fig. Appendix A.13). Apart from different iron oxides (e.g., magnetite Fe_3O_4 and hematite Fe_2O_3), we found different iron sulfides (e.g., pyrite FeS_2 and chalcopyrite $CuFeS_2$) (Fig. 11). The Paloma Norte samples, followed by the Olivares Alfa ones, show larger abundance and variability of iron-containing phases than those in the other samples (surface samples, Table 2). The metastable iron sulfate jarosite, the ferropotassic alunite endmember $KFe_2(SO_4)_2(OH)_6$, is present in the samples from Olivares Alfa, Paloma Norte, and Cerro Negro (Table 2). The stoichiometry is very close to the endmember. All other glacier samples do not include jarosite. We found iron sulfides (e.g., pyrite FeS_2 and Chalcopyrite $CuFeS_2$) for Olivares Alfa, Olivares Beta, Paloma Norte, and Cerro Negro (Table 2). The samples from the ice core show lower concentrations of stable iron

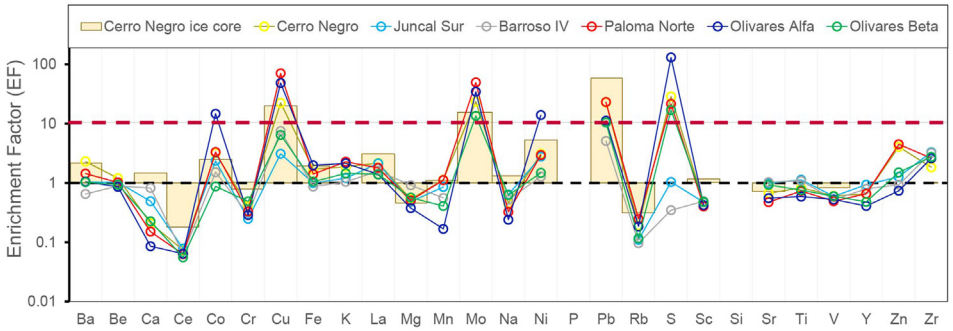

Fig. 9. Enrichment factors *EF* for different trace elements per glacier. Circles standing for *EFs* of surface samples, light yellow bars indicating average *EF* of ice core from Cerro Negro. Red dashed line showing *EF* of 10. All values above 10 likely caused by anthropogenic pollution; from 1 to 10, both natural and anthropogenic sources; below 1 (black dashed line), natural enrichment.

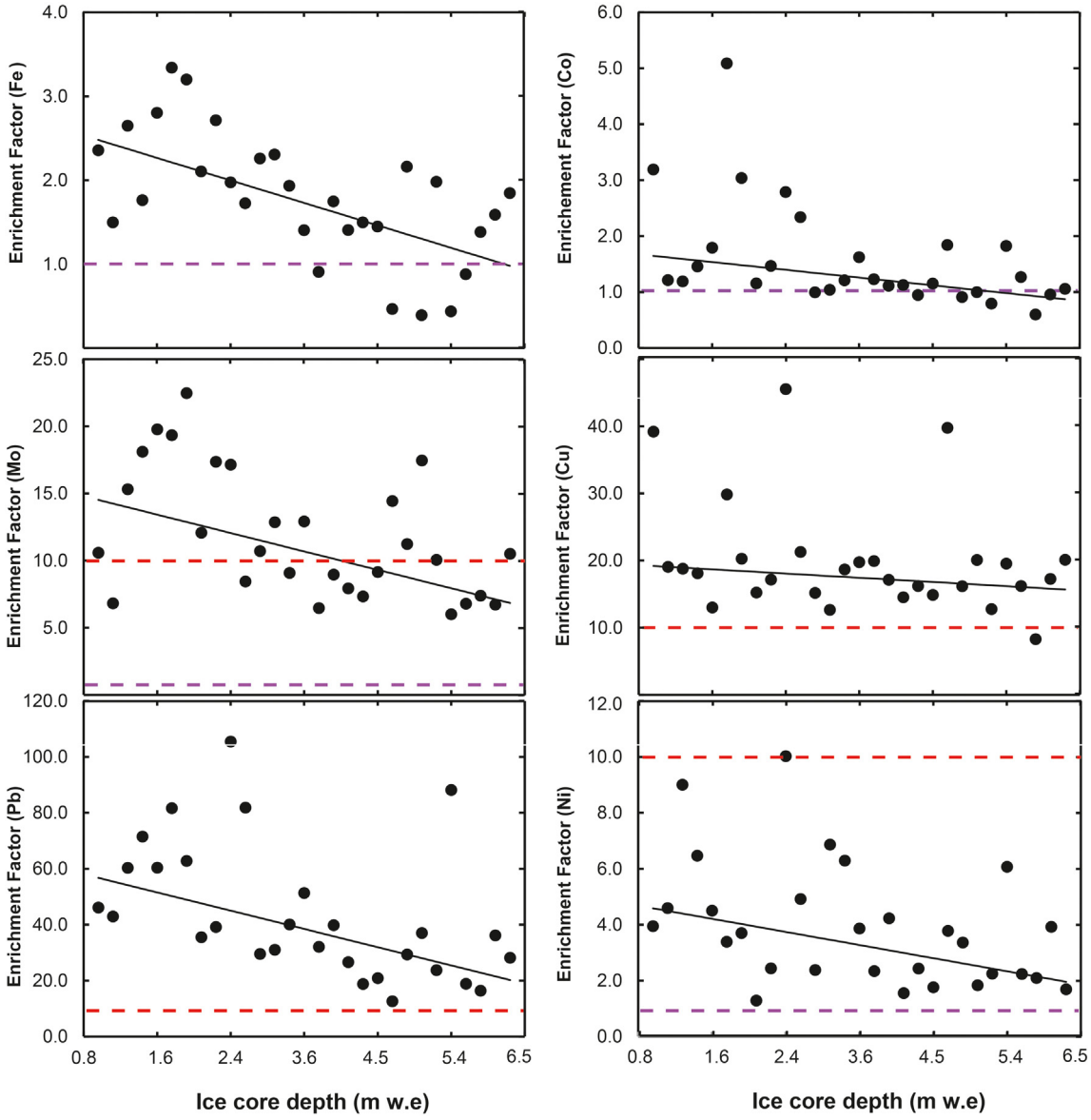

Fig. 10. Enrichment factors *EF* of each annual layer throughout ice core depth profile of selected trace elements from Cerro Negro. Uppermost 50 cm were not taken in account. The deeper the section of the core, the older the sample. Red dashed line indicating *EF* of 10 and purple dashed line, *EF* of 1.

oxides and iron sulfides in comparison with the surface samples (Table 2); however, we found higher concentrations of jarosite, especially in the deeper layers of the core (Table 2).

After analyzing the mineralogical composition, we were able to tie individual mineral grains to specific reflectance spectra at microscopic scale (Fig. 12). As expected, normalized reflectance spectra showed iron-containing minerals to have lower reflectance. Lowest reflectance values were found for iron sulfides (e.g., chalcopyrite $CuFeS_2$) and iron oxides, Fig. 12 and Appendix A.9).

5.4. Numerical modeling: across scales

5.4.1. Sensitivity of glacier melt to ice albedo changes

Our results show a strong linear relationship between melt and ice albedo (Fig. 13). The modeled mass balance rate agrees relatively well with the results reported by (Hugonnet et al., 2021, Fig. Appendix A.4). We found an average increase of melt sensitivity of +0.016 m w.e. for a change in mean ice albedo of −0.01. This is similar to the sensitivity of +0.014 m w.e. per −0.01 albedo decrease encountered for the Swiss Alps (Naegeli and Huss, 2017). The highest sensitivity was found for Paloma Norte (Table 3). Sensitivity to subseasonal snow albedo changes could not be assessed with the model used. However, we found good agreement between space-borne snow albedo changes over the winter season and a snow albedo decay parameterization by Oerlemans and Knap (1998) for all glaciers except for Paloma Norte (Fig. Appendix A.6). The sensitivity study clearly revealed the relation between glacier mass balance, corresponding melt rates, and surface albedo. This also revealed an increased mass balance sensitivity to a change in albedo for Paloma Norte and Olivares Alfa.

6. Discussion

6.1. Importance of mineral dust deposition on the glacier surface albedo

For all glaciers in the Olivares catchment, a considerable amount of LAIs ($\approx$70 g m^{-2} to $\approx$200 g m^{-2}) was detected. Yala Glacier in the Himalayas and Urumqi and July 1st Glacier in China (>200 g m^{-2}) present high dust concentrations (Takeuchi and Li, 2008), exceeding some of the LAI content

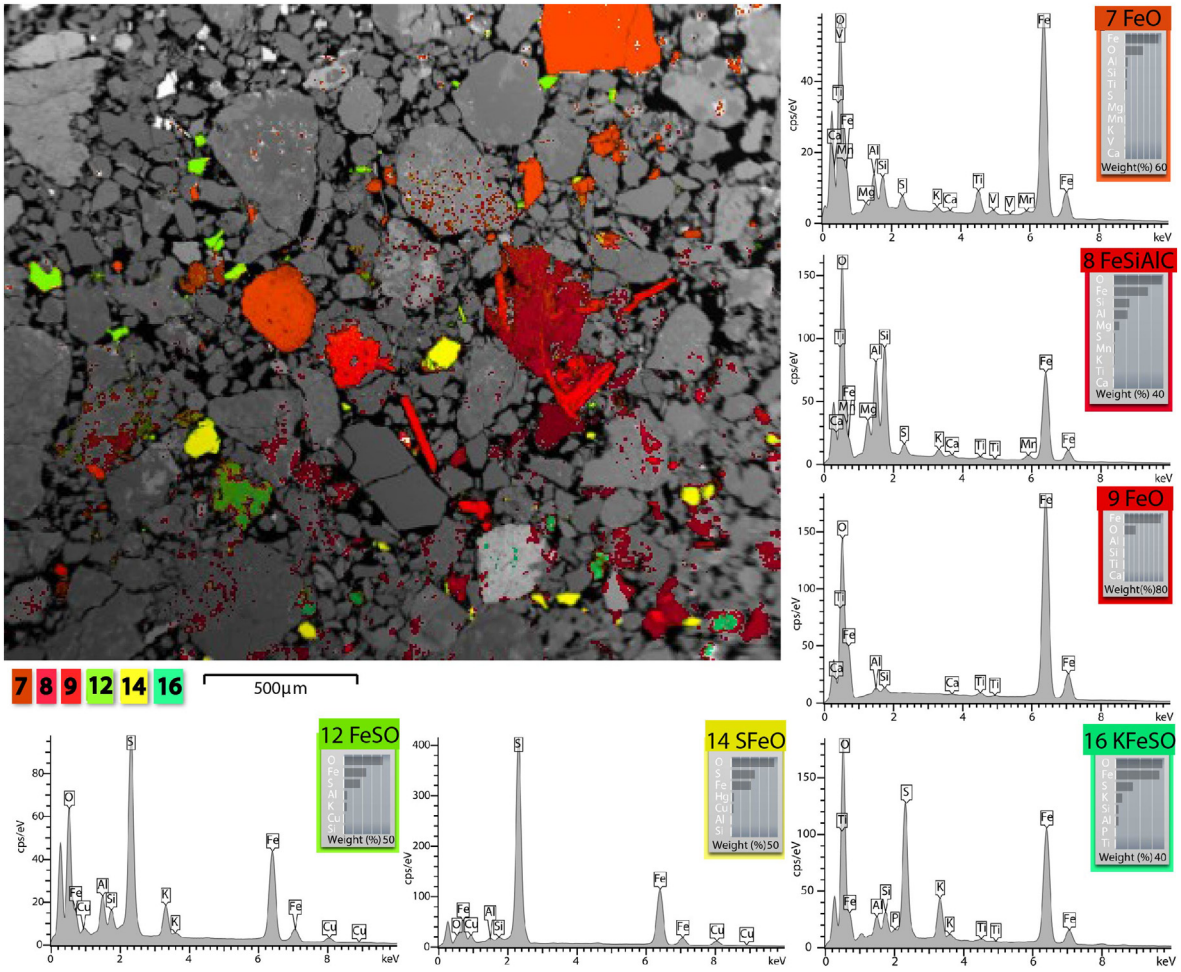

Fig. 11. Backscatter image of a polished section of Paloma Norte. The colors highlight element groups found in different fragments consisting of several phases. Element concentration extracted from each spectrum shown in the bar diagram insets. All fragments contain silicates (feldspars, phyllosilicates). Fragments corresponding to spectra 7–9 contain iron oxide/hydroxide as main phases (hematite, magnetite, or one of the (oxi)hydroxides), spectra 9 correspond to an almost pure iron oxide/hydroxide grain, spectrum 14 correspond to an almost pure iron sulfide (pyrite) (green and yellow: spectra 12, 14). The composition of the phase giving the spectrum 16 corresponds to the stoichiometry of jarosite. Examples for other glaciers shown in Appendix A.3.

found in the present work. Akkem Glacier in the Altay presents a similar amount of LAIs but higher OC concentrations than the glaciers studied in the present work (Takeuchi and Li, 2008). Despite the low reflectance of OC and BC (or EC) particles, their effect on albedo is reduced in the presence of a large quantity of high-absorbing mineral dust particles (Di Mauro et al., 2015; Kaspari et al., 2014) that capture part of the solar radiation that OC and BC would receive in the absence of mineral dust (Kaspari et al., 2011). Therefore, for environments in which mineral dust dominates LAI, mineral dust also dominates absorption, snow albedo reduction, and radiative forcing in snow (Di Mauro et al., 2015; Kaspari et al., 2014). This is relevant in particular for glaciers in the region studied in the present work, where most deposited LAIs are mineral dust particles (≈99%). We found that high-light-absorbing mineral dust particles are the most important LAIs controlling glacier surface albedo in the Olivares catchment.

6.2. Small-scale effect of LAIs on surface reflectance

Presence of debris and dust lowers reflectance in the lower spectral bands (<600 nm, Wiscombe and Warren, 1980) and is apparent through the strong absorption of solar radiation in the visible wavelength region for samples classified as dirty ice, ice with few debris, and cryoconites (Fig. 7). This reduction is less strong for the spectra of bright ice and more pronounced on Olivares Alfa and Paloma Norte. Highest reflectance corresponds to the bright ice class, which mostly corresponds to samples of the upper most layer of the weathering or refreezing crust. Formation of water ponds and cryoconite holes were observed below the weathering crust during the field visits. The effect of this near-surface material on the observed albedo, however, remains unexplained. At lower wavelengths, over 60% of solar radiation is reflected by the bright ice class. This is comparable to fresh snow, with a reflectance of up to 70% (Naegeli et al., 2017). Measurement of liquid water ponds and streams at the glacier surface show low reflectance, especially at higher wavelength (>800 nm), and can absorb up to 90% of solar radiation (Paul et al., 2005; Naegeli et al., 2015). Liquid water at the surface is more frequent below the snowline. We found iron oxide/hydroxide peaks in the reflectance spectra [at 430 nm and 535 (goethite) 555–575 nm (hematite), Wu et al., 2016], especially pronounced for the cryoconite (Fig. 4) and dirty ice samples from Olivares Alfa and Paloma Norte. Surface reflectance spectra obtained from Paloma Norte and the glacier tongue samples from Olivares Alfa show peaks indexed for iron oxide/hydroxide phases, whereas those obtained from Olivares Beta lack these peaks (Fig. 4). Wu et al. (2016) reports that the intensity of these peaks correlates with the quantity of the corresponding phases present. This together with the EDS elemental maps of the same samples suggest a higher iron-oxide/hydroxide content in LAIs for Olivares Alfa and Paloma Norte than for Olivares Beta; more importantly, this highlights the strong effect of minor LAIs components (iron oxides/hydroxides) on the measured surface ice reflectance spectra and consequently on the surface albedo of the glaciers at very small scale.

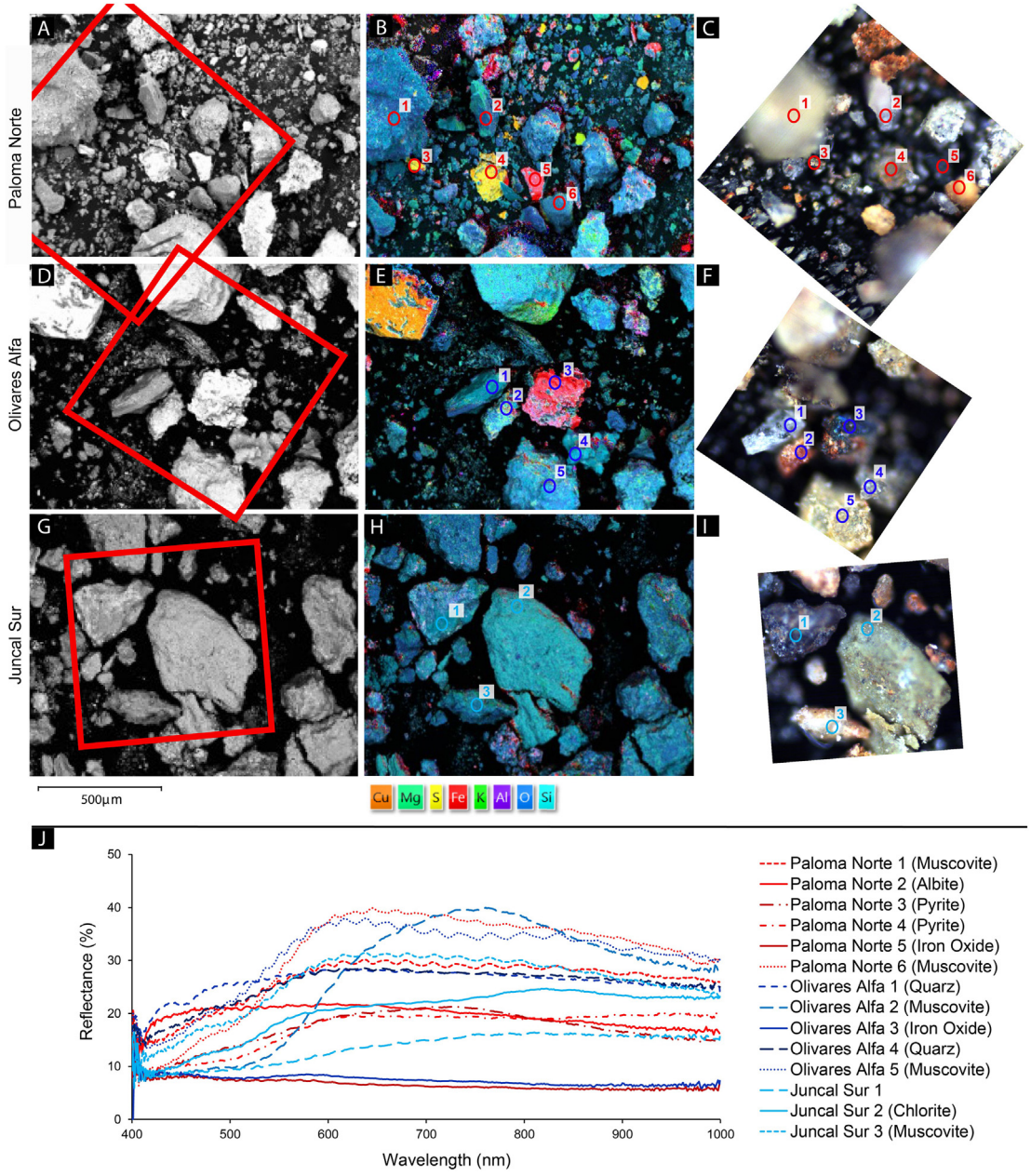

Fig. 12. Backscatter (BSE) and HIMS images of same areas of Paloma Norte A, Olivares Alfa D, and Juncal Sur G samples; the brighter the BSE images the higher the average atomic number of the phase(s). B, E and H show elemental maps for the same sample. Different elements coded by colors overlay (Cu = orange, Magnesium (Mg) = green, S = yellow, Fe = red, K = light green, Aluminium (Al) = purple, Oxygen (O) = 0 blue, Silicon (Si) = light blue). C, F, and I corresponding HIMS images. Circles with numbers indicating location of retrieval of normalized reflectance spectra shown in J.

6.3. The role of surface albedo change and glacier melt

Region- and glacier-wide end-of-summer albedo are in line with Shaw et al. (2021); detected changes are also similar to those in Peña and Olmedo (2019). Averaged ice albedo trends calculated below the snowline in Shaw et al. (2020) are based on a relatively small fraction of the total glacier area (5–30%), whereas in the present study, we report pixel-based trends. We did not average those trends over the entire glacier area due to unequal spatial coverage and distribution of the identified trends. Furthermore, average trends contain more information, mixing different processes into the signal, and thus hamper a process-oriented interpretation of the surface change signal (Naegeli et al., 2019). We found a darkening over the glacier tongues (Fig. 7) that is a result of changes in surface roughness (i.e., penitentes), different sources of dust deposition (Azzoni et al., 2014; Di Mauro et al., 2016; Di Mauro, 2020), development of cryoconite holes (Takeuchi et al., 2001; Cook et al., 2016), presence of water, and surface melt-out of particles incorporated in the deeper ice layers (Gomez and Small, 1985).

The encountered ice albedo trends at higher glacier elevation are complex and more heterogeneous (Fig. 7). We found positive trends for pixels just above the glacier snout for Paloma Norte, and starting from around the mean elevation upwards for Olivares Beta, Alfa, and Juncal Sur. These areas are all relatively flat, and processes such as sublimation, refreezing, and weathering crust formation may play a crucial role on the surface reflectance properties observed from space. Tedstone et al. (2020) found a strong impact of the state of the weathering crusts (i.e., density and

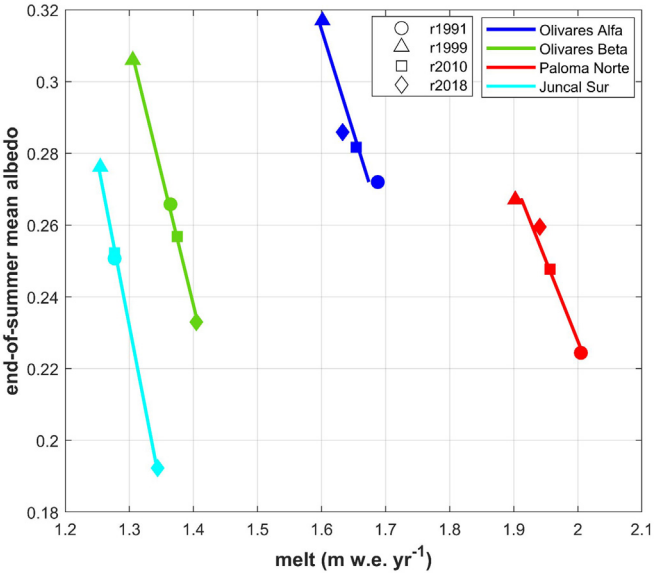

Fig. 13. Relationship between annual melt rates and mean end-of-summer glacier-wide albedo for different glaciers in study area.

porosity, interstitial, and ponded water content) on the surface albedo. Weathering crusts are more favorable to form on flat surfaces, under shortwave-dominant energy conditions and very low wind speeds, and are highly variable in space and time. Ayala et al. (2017) demonstrated the importance of wind speed to explain the spatial heterogeneity of melt and sublimation over the area of Juncal Norte. Measurements published in Codelco Chile (2019) highlight lower wind speeds on glacier than off glacier, especially from December to February. The measurement locations coincide with the locations of positive albedo change and demonstrate favorable conditions for surface crust formation. Schaefer et al. (2020) highlights the dominance of the incoming solar radiation in comparison with the other heat flux components for Bello glacier (located close by in the Colorado catchment). Increasing temperature and decreasing precipitation under the 10-year-long mega drought (Garreaud et al., 2020) could have produced a reduction of water vapor in the atmosphere. The missing water vapor, on the one hand, creates a stronger water-vapor gradient, enhancing sublimation and increasing penitentes growth and surface roughness; on the other hand, results in a diminution of the absorbed shortwave radiation in the atmosphere. A possible increase of incoming

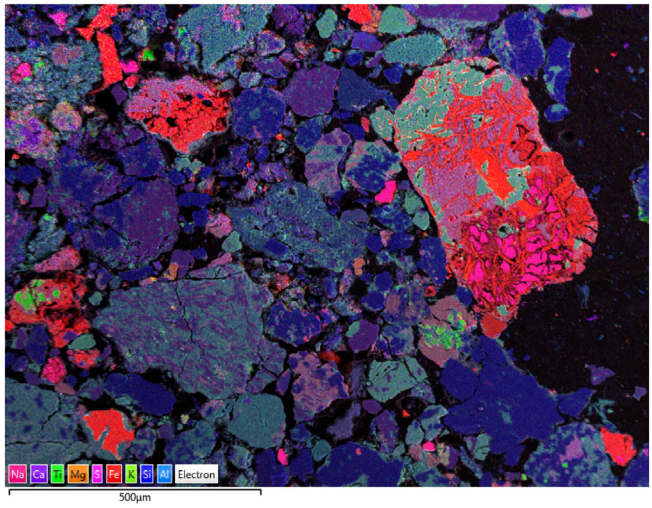

Fig. 14. EDS map of Paloma Norte sample showing rock particles with breccias typical texture.

Table 2
Percentage of iron-containing elements in the analyzed element maps classified into iron oxides, iron sulfides, and metastable iron sulfates jarosite for the different surface and ice core samples. The percentages represent the summarized abundance of all analyzed snapshots of each individual sample.

Sample location	Iron oxides	Iron sulfides	Jarosite
Paloma Norte	5.0%	1.0%	0.7%
Olivares Alfa	1–2%	1.5%	2.5%
Olivares Beta	1–2%	1.0%	–
Juncal Sur	1–2%	–	–
Barroso IV	1–2%	–	–
Cerro Negro$_{surface2019}$	5.5%	2.3%	0.3%
Cerro Negro$_{1961–2017}$	2.2%	1.7%	0.2%
Cerro Negro$_{1945}$	2.7%	1.7%	1.5%
Cerro Negro$_{1937}$	2.0%	1.8%	1.8%

solar radiation that penetrates the ice surface and the rime accretion at the surface, accelerated by cloud cover changes, could enhance melt within the upper ice layer. However, assessing those processes in detail lies beyond the scope of the present study. More effort is needed to reveal the processes behind the observed spatially heterogeneous albedo changes.

Enhanced subsurface melt in combination with low wind speed could favor weathering crust formation, characterized by high surface reflectance (reflectance spectra of bright ice). The development of a weathering crust enables LAIs to exert more control upon albedo, both directly and by modifying the optical parameters of the underlying ice surface via enhanced melt at patch scales (Tedstone et al., 2020). The increasing reflectance trends detected on satellite-based albedo maps, with a relatively low spatial resolution, show that such underlying small-scale effects remain undetected on larger scale assessments (Abermann et al., 2014). In situ surface reflectance measurements are therefore more suitable to disentangle the effect and interplay of different surface characteristics at smaller scale; however, time series of meaningful length are generally missing, and sample size is often not representative for the total glacier area. On microscopic level, we report that different LAIs compositions (i.e., increased deposition of iron-containing minerals) found for Paloma Norte and, to some degree, for Olivares Alfa lower the albedo of the samples. Quantifying these effects is difficult. The difficult scalability of the observed processes controlling surface albedo increasingly complicates the prediction of albedo changes and their effect on glacier mass balance in detail. The applied model cannot represent such small-scale spatio-temporal variability, and their influence on glacier melt remains unknown. Nevertheless, the use of spatially distributed albedo maps as input for modeling provides more detail of the enhanced albedo feedback that will be amplified due to atmospheric warming in the future (Abermann et al., 2014; Naegeli and Huss, 2017). A constant albedo value used for modeling can lead, especially at the glacier tongue, to a strong underestimation of melt rates (Naegeli and Huss, 2017).

6.4. The importance of snow albedo

The effect on glacier mass balance of the observed lower glacier-wide albedo at Juncal Sur and Olivares Beta during winter might be negligible. More important is the timing of the minimum glacier-wide albedo and its absolute value during summer time, principally governed by ice area extent. The accelerated seasonal glacier-wide albedo change for Paloma Norte and, to some extent, for Olivares Alfa is thus crucial (Fig. 6). This is a combination of faster snow depletion, LAIs deposition and snow aging, causing a feedback which leads to longer ablation seasons and, therefore, accelerated melt. We suggest that the earlier lowering of the surface albedo at Paloma Norte and Olivares Alfa explains an important part of the above-average mass loss over the past two decades reported in Dussaillant et al. (2019) and in Farías-Barahona et al. (2020).

The average snow albedo observed on satellite images at the end of different winters is very low, especially for Paloma Norte. Our modeling study suggests that the albedo decay parameterization failed to represent the seasonal snow albedo decrease at Paloma Norte, suggesting an additional

Table 3
Modeled mean annual surface mass balance ($SMB_{thisstudy}$) from 2000 to 2020 in comparison with observed geodetic mass balance $\Delta M_{2000-2018}$ in Dussaillant et al. (2019), $\Delta M_{2000-2013}$ in Farías-Barahona et al. (2020), and $\Delta M_{2000-2020}$ in Hugonnet et al. (2021). Also given: mass balance sensitivity to albedo α lowering of 0.01 (last column).

Glacier	$SMB_{thisstudy}$ (m w.e. yr^{-1})	$\Delta M_{2000-2018}$ (m w.e. yr^{-1})	$\Delta M_{2000-2013}$ (m w.e. yr^{-1})	$\Delta M_{2000-2020}$ (m w.e. yr^{-1})	Change in melt (m w.e. $-0.01\Delta\alpha^{-1}$)
Juncal Sur	−0.30 ± 0.12	−0.27 ± 0.03	−0.26 ± 0.11	−0.29 ± 0.11	+0.011
Olivares Beta	−0.51 ± 0.15	−0.43 ± 0.05	−0.24 ± 0.11	−0.54 ± 0.11	+0.014
Olivares Alfa	−0.72 ± 0.19	−0.85 ± 0.09	−0.88 ± 0.11	−0.83 ± 0.15	+0.017
Paloma Norte	−1.05 ± 0.26	−0.97 ± 0.11		−1.06 ± 0.22	+0.022

source for albedo decay, such as enhanced LAI deposition. We observed a strong albedo reduction at the northern flank of the glacier tongue, close to the location of PN04 (Fig. 2). Field spectrometer measurement at PN04 showed the lowest reflectance reported for the ice samples for Paloma Norte (Fig. 7). Thus, the observed early snow albedo reduction might relate to a localized increase of LAI deposition. Sources of mineral dust are eroding rocks (including water and ice as erosion agents) or wind-transported material. Larger debris fragments can only reach the actual location through gravitational transport onto the glacier surface. Smaller particles (aerosol <100 μm in size), however, can be transported by wind. In the ice surface samples at Paloma Norte, we found strongly light-absorbing rock particles with a texture typical for breccias found in the pipes exploited by the mines (Fig. 14) and jarosite particles. Due to the topographic and geological setting, these particles are not expected to be mobilized or produced through erosion and deposited on the glacier surface through natural processes. Jarosite can only form and survive in the mine tailings; breccia outcrops are only present topographically below the studied glacier, in the mining area. Both can reach the northeastern part of Paloma Norte only through wind transport from the mine tailings. Measurements of wind direction show that ascending winds over the mining area reach the northeastern flank of Paloma Norte (Fig. 2, Codelco Chile, 2019). Codelco Chile (2019) also reports winds from this direction to be strongest during autumn and winter. However, these winds are weak at the northeastern part of the glacier, where descending winds from the southwest are stronger. The descending winds from southeast to northwest dominate the entire glacier during spring and summer (Codelco Chile, 2019). For Olivares Alfa, measurements show that the ascending winds over the mine area reach the glacier tongue from the north and propagate upwards to the accumulation area, where they weaken (Codelco Chile, 2019). Measurements of wind-direction-dependent aerosol transport at Olivares Alfa (from Direccion General de Aguas) from October 21 to October 29, 2014 recorded a strong increase of the two particular matter (PM) classes with aerodynamic diameters not larger than 2.5 μm (PM2.5) and 10.0 μm (PM10) for wind directions from northwest to southeast. These findings support our results and suggest that particles mobilized from the loose dust deposits of the mine tailings could reach the tongue of Paloma Norte and the ablation area of Olivares Alfa, especially during the winter season, and might produce an important seasonal snow albedo reduction during the winter months for the two sites.

6.5. Evidence of anthropogenic pollution

Iron oxides, hydroxides, sulfides, and sulfates are efficient light-scattering and light-absorbing materials, which can enhance absorption at ultra violet and visible wavelengths (Zhang et al., 2015). Small-scale variability of the surface albedo may be due to different iron oxide and sulfide content in the dust particles. The percentage of iron-containing minerals in the element maps based on SEM measurements are somewhat lower for Juncal Sur and Barroso IV, similar for Olivares Beta, but considerably higher for Olivares Alfa, Paloma Norte, and Cerro Negro (up to ≈8%, Table 2). Wu et al. (2016) found values reaching 4.32% of iron content in LAIs in firn cores from different glaciers in High Asia; Shi et al. (2011) reported values up to 5.7%. The here encountered iron concentration in the surface samples is approximately 1.5 times higher for Paloma Norte, Cerro Negro, and Olivares Alfa than for Barroso IV, Olivares Beta, and Juncal Sur. The first three lie within the range of the values encountered for the Coastal Cordillera of northern Chile (≈6.0%, Oliveros et al., 2007), while the latter three have substantially lower iron concentrations. Material from the pyrite-containing hydrothermal alteration zones (Section 2.2 and Appendix A.1.1) can reach Paloma Norte, Olivares Alfa, and Beta by gravitation, water and ice transport, and wind transport. This might partly explain the higher iron concentration in the surface samples in comparison with Juncal Sur and Olivares Beta. However, iron concentrations increased over time at Cerro Negro, and the calculated *EF* shows a significant positive trend at a 99% level. *EF* of deeper ice core samples suggests natural occurrence. The more recent layers (closer to the surface) suggest some anthropogenic influence on the iron concentration (*EF*: 1 to 10, Fig. 10).

Along the variable iron concentration, enriched trace elements suggest an anthropogenic influence (Cu, Pb, Mo, La, and Ni). Cereceda-Balic et al. (2012) identified traffic, smelting, biomass, coal burning, and waste incineration as sources for enriched trace elements in snow at the nearby Cerro Colorado. Our study shows that the enrichment of these trace elements has increased since the 1920s. The contrast between the enrichment factors of the sample sites located at close proximity to the mining area (Paloma Norte, Olivares Alfa, and Cerro Negro) and those from the glaciers situated further away from the mines (Juncal Sur, Barroso IV, and Olivares Beta) is striking. Alfonso et al. (2019) found significant anthropogenic enrichment of copper and molybdenum in samples at a distance of about 15 km to the copper mines Los Bronces and Andina. Our results accredit anthropogenic enrichment of the same elements at Olivares Alfa and Paloma Norte (*EF* > 50).

We found jarosite at Olivares Alfa, Paloma Norte, and in the samples from Cerro Negro (Table 2). Dold and Fontboté (2001) found jarosite in the mine tailings. Material from these tailings can only be transported to the glaciers by wind and cannot form at the natural environment of the Olivares catchment. Thus, jarosite must have been transported in the form of aerosol from these tailing sites onto the glacier surfaces, as it cannot form in situ because the pH of melt water from the glacier is too high. Jarosite is metastable and decomposes in the presence of humidity/liquid water to iron hydroxide. Its presence in the Cerro Negro core suggests burying of the jarosite with snow in the accumulation area at the ice core drill site (Table 2).

More evidence of the transport of aerosols from the mine tailings onto the glacier surface is the higher fossil EC concentration at Paloma Norte compared with Olivares Alfa samples (Fig. Appendix A.7) and the breccia particles (Fig. 14).

6.6. Limitations

A major limitation of the present study is the representativeness of our results; so is tying them across scales. Sample sites are distributed over the glacier area but restricted to well accessible sites. The different chemical and mineralogical analyses of those samples are labor and cost intensive and were thus limited to a selection only.

In situ reflectance measurements for a field of 4 × 4 m are not straightforward for a penitentes-dominated glacier surface; consequently, our measurements tended to be taken on flatter ground. Surface type classification is based on expert knowledge. To compare albedo derived from Landsat satellite images with direct field observations is difficult due to different measured spectral ranges and spatial resolution (Naegeli et al., 2017). Weathering crust formation, sublimation, refreezing, and thaw-freeze

cycles are diurnal processes that cause temporal variability of the surface albedo; these processes could not be captured with the data used in this study. Similarly, the effect of the reduction of reflectance intensity of mineral grains is difficult to quantify on glacier scale; so is to quantitatively link satellite-based observations with small-scale albedo variations.

Our results highlight anthropogenic LAIs sources and modification of their composition, concentration, and distribution; however, quantifying the amount of natural and anthropogenic mineral dust loads mobilized and deposited on the glacier surface remains a challenge. The mining waste deposits provide a source for various minerals that can be wind-transported apart from the particles that we identified as mobilized and originated in the mine area (jarosite, breccia). In the present work, we were not able to separate pure nonmining-affected dust mobilization nor quantify the effect of LAIs deposition originating from the mining area on the glacier-wide mass balance. Our evidence of mining residuals on the glaciers is based on the chemical and mineralogical compositions of dust particles collected on the glacier surface and in the ice core, rather than on a back trajectory analysis. Such analysis, in combination with wind-directed aerosol measurements, could provide important insights into the wind redistribution patterns of LAIs and facilitate the quantification of the actual amount of anthropogenic LAIs deposited on the glaciers in the region.

The model used in the present study delivers a first, strongly parameterized (e.g., constant lapse rates) estimate and is not able to reflect all relevant physical processes, such as sublimation, snow aging, formation of penitentes, or diurnal variations. The model uses distributed ice albedo from satellite scenes. This can better represent the spatio-temporal heterogeneity of glacier mass balance - albedo interaction compared with conventional modeling using a constant albedo values for snow, firn, and ice (Naegeli and Huss, 2017). However, it remains restricted to annual albedo heterogeneity on a pixel size of 30 m. Smaller scale heterogeneity is thus not represented. Furthermore, the snow albedo decrease is based on a strongly parameterized scheme. The choice of the model responds to a lack of available model input data. Nevertheless, we believe our approach provides a valuable first-order estimate of surface melt sensitivity to glacier ice albedo changes because we used distributed ice albedo maps. The modeling approach cannot reveal the detailed underlying processes. Future studies need to include not only distributed ice albedo but also snow albedo variations throughout the accumulation season and a more physical-based mass balance model.

7. Conclusion

Up to 99% of LAIs collected in the Olivares catchment are mineral dust particles. Iron-containing particles lower the glacier surface reflectance and are more frequent on the glacier surface at Olivares Alfa and Paloma Norte. Minor LAIs components (iron oxides/hydroxides) have a strong effect on the surface reflectance properties of the glaciers. Trace elements are significantly enriched at the surface of Olivares Alfa, Paloma Norte, and Cerro Negro (closest to the mines) compared with the natural occurrence found at Juncal Sur and Barroso IV (further from the mines). An increase in enrichment factors is apparent at the Cerro Negro ice core location since the 1920s. Large-scale assessment from satellite-based observations reveals ice albedo lowering (darkening) at most glacier tongues from 1989 to 2018. However, pixel-based albedo trends are heterogeneous, especially above the median glacier elevation. This might relate to increased formation of weathering crusts at the ice surfaces because of changes in atmospheric conditions related to the mega drought. Glacier melt, in particular for Paloma Norte, is very sensitivity to ice albedo changes. However, differences in ice albedo alone cannot explain the above-average mass loss observed at Paloma Norte and Olivares Alfa. Surface dust depositions influence winter snow albedo decrease, prolonging the exposure of low-reflective ice areas. This can explain the above-average loss balances found in the catchment. However, we were not able to model the observed snow albedo decay with our modeling approach. Our results suggest that mechanisms and feedbacks other than the mega drought (Garreaud et al., 2017) are driving the above-average negative glacier mass balance of Paloma Norte and Olivares Alfa (glaciers close to the mines). These processes change surface characteristics such as LAIs distribution pattern, changing snow and ice albedo and their evolution over time, from very small to regional scale. Some processes responsible for changing the surface characteristics of the glaciers have a natural origin, such as land cover degradation exposing soil to erosion and intensive dust particle mobilization (e.g. Shepherd et al., 2016; Al Ameri et al., 2019). Others have an anthropogenic origin or relate to anthropogenic activities and are linked to mining activities in the Andina and Los Bronces mines. This anthropogenic influence includes the enrichment of trace elements and the increased dust mobilization and deposition on the glacier surface due to the mobilization of loose material from the nearby mine tailing. However, we were not able to provide quantitative estimates of the glacier-wide contribution from either natural or anthropogenic LAIs sources.

We present clear evidence of mineral particles mobilized by mining activities having been transported and deposited on the glaciers surface: (1) jarosite formed only in the mine tailings and (2) particles with breccia typical structure found at the glacier surface. Those particles have been transported from the mining area in agreement with the dominant wind patterns and aerosol monitoring. We conclude that the nearby copper mines provide a source for LAIs deposited at the glacier surface. Mass balance and associated melt volumes are sensitive to ice albedo. The effect of LAIs on surface albedo and the sensitivity of glacier mass balance to changes therein are highly complex and strongly analysis-scale dependent.

CRediT authorship contribution statement

M. Barandun: Ceptualization; Data curation; Formal analysis; Investigation; Methodology; Validation; Visualization; Roles/Writing – original draft.

C. Bravo: Data curation; Formal analysis; Methodology; Visualization; Writing – review & editing.

B. Grobety: Formal analysis; Methodology; Supervision; Writing – review & editing.

T. Jenk: Data curation; Formal analysis; Investigation; Methodology; Visualization; Writing – review & editing.

L. Fang: Data curation; Formal analysis; Investigation; Methodology; Writing – review & editing.

K. Naegeli: Methodology; Writing – review & editing.

A. Rivera: Conceptualization; Funding acquisition; Supervision; Writing – review & editing.

S. Cisternas: Data curation; Writing – review & editing.

T. Münster: Data curation; Formal analysis.

M. Schwikowski: Conceptualization; Funding acquisition; Supervision; Writing – review & editing.

Declaration of competing interest

We do not have any conflict of interest.

Acknowledgements

We thank S. Koechli for performing the sample preparation and the ICP-OES measurements; D. Farias for the geodetic mass balance and elevation change data at Cerro Negro to deduce surface change for the location of the drill site. This research has been funded with a fellowship from the Glaciologia y Cambio Climatico Centro de Estudios Cientificos (CECs) Valdivia Chile. We thank T. Saks for advice on geological data interpretation. We thank the two anonymous reviewers for their constructive comments.

Appendix A. Supplementary data

Supplementary data to this article can be found online at https://doi.org/10.1016/j.scitotenv.2022.155068.

References

Abermann, J., Kinnard, C., MacDONELL, S., 2014. Albedo variations and the impact of clouds on glaciers in the Chilean semi-arid Andes. J. Glaciol. 60, 183–191.

Al Ameri, I.D., Briant, R.M., Engels, S., 2019. Drought severity and increased dust storm frequency in the middle east: a case study from the Tigris–Euphrates Alluvial Plain, Central Iraq. Weather 74, 416–426.

Alfonso, J.A., Cordero, R.R., Rowe, P.M., Neshyba, S., Casassa, G., Carrasco, J., MacDonell, S., Lambert, F., Pizarro, J., Fernandoy, F., et al., 2019. Elemental and mineralogical composition of the western Andean snow (18° s–41° s). Sci. Rep. 9, 1–13.

Avak, S.E., Schwikowski, M., Eichler, A., 2018. Impact and implications of meltwater percolation on trace element records observed in a high-alpine ice core. J. Glaciol. 64, 877–886.

Ayala, A., Pellicciotti, F., MacDonell, S., McPhee, J., Vivero, S., Campos, C., Egli, P., 2016. Modelling the hydrological response of debris-free and debris-covered glaciers to present climatic conditions in the semiarid Andes of central Chile. Hydrol. Process. 30, 4036–4058.

Ayala, A., Pellicciotti, F., Peleg, N., Burlando, P., 2017. Melt and surface sublimation across a glacier in a dry environment: distributed energy-balance modelling of Juncal Norte Glacier, Chile. J. Glaciol. 63, 803–822.

Ayala, Á., Farías-Barahona, D., Huss, M., Pellicciotti, F., McPhee, J., Farinotti, D., 2020. Glacier runoff variations since 1955 in the Maipo River Basin, in the semiarid Andes of central Chile. Cryosphere 14, 2005–2027.

Azzoni, R., Senese, A., Zerboni, A., Maugeri, M., Smiraglia, C., Diolaiuti, G., 2014. A novel integrated method to describe dust and fine supraglacial debris and their effects on ice albedo: the case study of Forni Glacier, Italian Alps. Cryosphere Discuss. 8, 3171–3206.

Barandun, M., Pohl, E., Naegeli, K., McNabb, R., Huss, M., Berthier, E., Saks, T., Hoelzle, M., 2021. Hot spots of glacier mass balance variability in central Asia. Geophys. Res. Lett. 48 (11), e2020GL092084.

Barraza, F., Lambert, F., MacDonell, S., Sinclair, K., Fernandoy, F., Jorquera, H., 2021. Major atmospheric particulate matter sources for glaciers in Coquimbo region, Chile. Environ. Sci. Pollut. Res. 1–11.

Beach, J.M., Uertz, J.L., Eckhardt, L.G., 2015. Hyperspectral interferometry: sizing microscale surface features in the pine bark beetle. Microsc. Res. Tech. 78, 873–885.

Bish, D.L., Post, J.E., 1993. Quantitative mineralogical analysis using the Rietveld full-pattern fitting method. Am. Mineral. 78, 932–940.

Boisier, J.P., Alvarez-Garreton, C., Cordero, R.R., Damiani, A., Gallardo, L., Garreaud, R.D., Lambert, F., Ramallo, C., Rojas, M., Rondanelli, R., et al., 2018. Anthropogenic drying in central-southern Chile evidenced by long-term observations and climate model simulations. Elementa6.

Box, J.E., Fettweis, X., Stroeve, J.C., Tedesco, M., Hall, D.K., Steffen, K., 2012. Greenland ice sheet albedo feedback: thermodynamics and atmospheric drivers. Cryosphere 6, 821–839. https://doi.org/10.5194/tc-6-821-2012 URL: https://tc.copernicus.org/articles/6/821/2012/.

Braun, M.H., Malz, P., Sommer, C., Farías-Barahona, D., Sauter, T., Casassa, G., Soruco, A., Skvarca, P., Seehaus, T.C., 2019. Constraining glacier elevation and mass changes in South America. Nat. Clim. Chang. 9, 130–136.

Brenning, A., 2008. The impact of mining on rock glaciers and glaciers. In: Orlove, B., Wiegandt, E., Luckman, B. (Eds.), Darkening Peaks: Glacier Retreat, Science, And Society. University of California, Berkeley, pp. 196–205.

Brenning, A., Azócar, G.F., 2010. Minería y glaciares rocosos: impactos ambientales, antecedentes politicos y legales, y perspectivas futuras. Rev.Geogr.Norte Grande 143–158.

Brock, B.W., Willis, I.C., Sharp, M.J., 2000. Measurement and parameterization of albedo variations at haut glacier d'arolla, Switzerland. J. Glaciol. 46, 675–688. https://doi.org/10.3189/172756500781832675.

Brun, F., Dumont, M., Wagnon, P., Berthier, E., Azam, M.F., Shea, J.M., Sirguey, P., Rabatel, A., Ramanathan, A., 2015. Seasonal changes in surface albedo of Himalayan glaciers from MODIS data and links with the annual mass balance. Cryosphere 9, 341–355. https://doi.org/10.5194/tc-9-341-2015 URL: https://tc.copernicus.org/articles/9/341/2015/.

Burger, F., Brock, B., Montecinos, A., 2018. Seasonal and elevational contrasts in temperature trends in central Chile between 1979 and 2015. Glob. Planet. Chang. 162, 136–147.

Cereceda-Balic, F., Palomo-Marín, M., Bernalte, E., Vidal, V., Christie, J., Fadic, X., Guevara, J., Miro, C., Gil, E.P., 2012. Impact of Santiago de Chile urban atmospheric pollution on anthropogenic trace elements enrichment in snow precipitation at Cerro Colorado, Central Andes. Atmos. Environ. 47, 51–57.

Cereceda-Balic, F., Funes, M.Z.n.R., Vidal, V., Fadic, R., Muñoz, J., Acuña, J., Reinoso, C., Llanos, P., 2014. Glacio-chemical characterisation of trace elements in snow samples (in Spanish).

Cereceda-Balic, F., Ruggeri, M., Vidal, V., 2020. Glacier retreat differences in Chilean Central Andes and their relation with anthropogenic black carbon pollution. 2020 IEEE Latin American GRSS & ISPRS Remote Sensing Conference (LAGIRS). IEEE, pp. 434–440.

Codelco Chile, División Andina, 2019. In: Cuadra Pesce, Roberto Alejandro (Ed.), Adecuaci/on obras mineras de andina para continuidad operacional actual, 11. Capitulo 3.11 glaciares.Estudio de Impacto Ambiental, Codelco Chile

Cook, J., Edwards, A., Takeuchi, N., Irvine-Fynn, T., 2016. Cryoconite: the dark biological secret of the cryosphere. Prog. Phys. Geogr. 40, 66–111.

Cook, J.M., Hodson, A.J., Gardner, A.S., Flanner, M., Tedstone, A.J., Williamson, C., Irvine-Fynn, T.D., Nilsson, J., Bryant, R., Tranter, M., 2017. Quantifying bioalbedo: a new physically based model and discussion of empirical methods for characterising biological influence on ice and snow albedo. Cryosphere 11, 2611–2632.

Dal Farra, A., Kaspari, S., Beach, J., Bucheli, T.D., Schaepman, M., Schwikowski, M., 2018. Spectral signatures of submicron scale light-absorbing impurities in snow and ice using hyperspectral microscopy. J. Glaciol. 64, 377–386.

Deckart, K., Clark, A.H., Celso, A.A., Ricardo, V.R., Bertens, A.N., Mortensen, J.K., Fanning, M., 2005. Magmatic and hydrothermal chronology of the Giant Río Blanco porphyry copper deposit, Central Chile: implications of an integrated U-Pb and 40Ar/39Ar database. Econ. Geol. 100, 905–934.

Deckart, K., Clark, A.H., Cuadra, P., Fanning, M., 2013. Refinement of the time-space evolution of the giant Mio-Pliocene Río Blanco-Los Bronces porphyry Cu–Mo cluster, Central Chile: new U–Pb (shrimp ii) and Re–Os geochronology and 40 Ar/39 Ar thermochronology data. Mineral. Deposita 48, 57–79.

Di Mauro, B., 2020. A darker cryosphere in a warming world. Nat. Clim. Chang. 10, 979–980.

Di Mauro, B., Fava, F., Ferrero, L., Garzonio, R., Baccolo, G., Delmonte, B., Colombo, R., 2015. Mineral dust impact on snow radiative properties in the European alps combining ground, UAV, and satellite observations. J.Geophys.Res.Atmos. 120, 6080–6097.

Di Mauro, B., Julitta, T., Colombo, R., 2016. Glacier albedo decrease in the european alps: potential causes and links with mass balances. EGU General Assembly Conference Abstracts pp. EPSC2016–9746.

Dold, B., 2003. Dissolution kinetics of schwertmannite and ferrihydrite in oxidized mine samples and their detection by differential x-ray diffraction (dxrd). Appl. Geochem. 18, 1531–1540.

Dold, B., Fontbot/e, L., 2001. Element cycling and secondary mineralogy in porphyry copper tailings as a function of climate, primary mineralogy, and mineral processing. J. Geochem. Explor. 74, 3–55.

Dussaillant, I., Berthier, E., Brun, F., Masiokas, M., Hugonnet, R., Favier, V., Rabatel, A., Pitte, P., Ruiz, L., 2019. Two decades of glacier mass loss along the Andes. Nat. Geosci. 12, 802–808.

Eichler, A., Gramlich, G., Kellerhals, T., Tobler, L., Rehren, T., Schwikowski, M., 2017. Ice-core evidence of earliest extensive copper metallurgy in the Andes 2700 years ago. Sci. Rep. 7, 1–11.

El-Zanan, H.S., Lowenthal, D.H., Zielinska, B., Chow, J.C., Kumar, N., 2005. Determination of the organic aerosol mass to organic carbon ratio in improve samples. Chemosphere 60, 485–496.

Falvey, M., Garreaud, R.D., 2009. Regional cooling in a warming world: recent temperature trends in the southeast Pacific and along the west coast of subtropical South America (1979–2006). J.Geophys.Res.Atmos. 114.

Farías-Barahona, D., Vivero, S., Casassa, G., Schaefer, M., Burger, F., Seehaus, T., Iribarren-Anacona, P., Escobar, F., Braun, M.H., 2019. Geodetic mass balances and area changes of Echaurren Norte Glacier (central Andes, Chile) between 1955 and 2015. Remote Sens. 11, 260.

Farías-Barahona, D., Ayala, Á., Bravo, C., Vivero, S., Seehaus, T., Vijay, S., Schaefer, M., Buglio, F., Casassa, G., Braun, M.H., 2020. 60 years of glacier elevation and mass changes in the Maipo River Basin, Central Andes of Chile. Remote Sens. 12, 1658.

Gäggeler, H., Von Gunten, H., Rossler, E., Oeschger, H., Schotterer, U., 1983. 210Pb-dating of cold alpine firn/ice cores from Colle Gnifetti, Switzerland. J. Glaciol. 29, 165–177.

Gäggeler, H.W., Tobler, L., Schwikowski, M., Jenk, T.M., 2020. Application of the radionuclide 210Pb in glaciology–an overview. J. Glaciol. 66, 447–456.

Garreaud, R., 2009. The Andes climate and weather. Adv. Geosci. 22, 3–11.

Garreaud, R.D., Vuille, M., Compagnucci, R., Marengo, J., 2009. Present-day South American climate. Palaeogeogr. Palaeoclimatol. Palaeoecol. 281, 180–195.

Garreaud, R., Lopez, P., Minvielle, M., Rojas, M., 2013. Large-scale control on the Patagonian climate. J. Clim. 26, 215–230.

Garreaud, R.D., Alvarez-Garreton, C., Barichivich, J., Boisier, J.P., Christie, D., Galleguillos, M., LeQuesne, C., McPhee, J., Zambrano-Bigiarini, M., 2017. The 2010–2015 megadrought in Central Chile: impacts on regional hydroclimate and vegetation. Hydrol. Earth Syst. Sci. 21, 6307–6327.

Garreaud, R.D., Boisier, J.P., Rondanelli, R., Montecinos, A., Sepúlveda, H.H., Veloso-Aguila, D., 2020. The Central Chile mega drought (2010–2018): a climate dynamics perspective. Int. J. Climatol. 40, 421–439.

Gomez, B., Small, R., 1985. Medial moraines of the haut glacier d'Arolla, Valais, Switzerland: debris supply and implications for moraine formation. J. Glaciol. 31, 303–307.

Hansen, J., Nazarenko, L., 2004. Soot climate forcing via snow and ice albedos. Proc. Natl. Acad. Sci. 101, 423–428.

Hugonnet, R., McNabb, R., Berthier, E., Menounos, B., Nuth, C., Girod, L., Farinotti, D., Huss, M., Dussaillant, I., Brun, F., et al., 2021. Accelerated global glacier mass loss in the early twenty-first century. Nature 592, 726–731.

Huneeus, N., Lapere, R., Mazzeo, A., Ordóñez, C., Donoso, N., Muñoz, R., Rutllant, J.A., 2021. Deep winter intrusions of urban black carbon into a canyon near Santiago, Chile: a pathway towards Andean glaciers. Environ. Pollut. 291, 118124.

Huss, M., Hock, R., 2018. Global-scale hydrological response to future glacier mass loss. Nat. Clim. Chang. 1.

Huss, M., Bookhagen, B., Huggel, C., Jacobsen, D., Bradley, R., Clague, J., Vuille, M., Buytaert, W., Cayan, D., Greenwood, G., et al., 2017. Toward mountains without permanent snow and ice. Earth's Future 5, 418–435.

Jarvis, A., Reuter, H.I., Nelson, A., Guevara, E., et al., 2008. Hole-filled srtm for the globe version 4. available from the CGIAR-CSI SRTM 90m Database http://srtm.csi.cgiar.org 15.

Kaspari, S.D., Schwikowski, M., Gysel, M., Flanner, M., Kang, S., Hou, S., Mayewski, P.A., 2011. Recent increase in black carbon concentrations from a Mt.Everest ice core spanning 1860–2000 ad. Geophys. Res. Lett. 38.

Kaspari, S., Painter, T.H., Gysel, M., Skiles, S., Schwikowski, M., 2014. Seasonal and elevational variations of black carbon and dust in snow and ice in the Solu-Khumbu, Nepal and estimated radiative forcings. Atmos. Chem. Phys. 14, 8089–8103.

Kendall, M.G., 1948. Rank Correlation Methods.

Klok, E., Oerlemans, J., 2004. Modelled climate sensitivity of the mass balance of morteratschgletscher and its dependence on albedo parameterization. Int.J.Climatol. 24, 231–245.

Lapere, R., Mailler, S., Menut, L., Huneeus, N., 2021. Pathways for wintertime deposition of anthropogenic light-absorbing particles on the Central Andes cryosphere. Environ. Pollut. 272, 115901.

Lavanchy, V., Gäggeler, H., Nyeki, S., Baltensperger, U., 1999. Elemental carbon (ec) and black carbon (bc) measurements with a thermal method and an aethalometer at the high-alpine research station Jungfraujoch. Atmos. Environ. 33, 2759–2769.
Liang, S., 2001. Narrowband to broadband conversions of land surface albedo i: algorithms. Remote Sens. Environ. 76, 213–238.
Lucht, W., Hyman, A.H., Strahler, A.H., Barnsley, M.J., Hobson, P., Muller, J.P., 2000. A comparison of satellite-derived spectral albedos to ground-based broadband albedo measurements modeled to satellite spatial scale for a semidesert landscape. Remote Sens. Environ. 74, 85–98.
Madden, M.E., Bodnar, R., Rimstidt, J., 2004. Jarosite as an indicator of water-limited chemical weathering on mars. Nature 431, 821–823.
Malmros, J.K., Mernild, S.H., Wilson, R., Yde, J.C., Fensholt, R., 2016. Glacier area changes in the central Chilean and Argentinean Andes 1955–2013/14. J. Glaciol. 62, 391–401.
Mann, H.B., 1945. Nonparametric tests against trend. Econometrica 245–259.
Mardones, P., Garreaud, R.D., 2020. Future changes in the free tropospheric freezing level and rain–snow limit: the case of Central Chile. Atmosphere 11, 1259.
Masek, J.G., Vermote, E.F., Saleous, N.E., Wolfe, R., Hall, F.G., Huemmrich, K.F., Gao, F., Kutler, J., Lim, T.K., 2006. A Landsat surface reflectance dataset for North America, 1990–2000. IEEE Geosci. Remote Sens. Lett. 3, 68–72.
Masiokas, M.H., Christie, D.A., Le Quesne, C., Pitte, P., Ruiz, L., Villalba, R., Luckman, B.H., Berthier, E., Nussbaumer, S.U., González-Reyes, Á., et al., 2016. Reconstructing the annual mass balance of the Echaurren Norte Glacier (central Andes, 33.5 s) using local and regional hydroclimatic data. Cryosphere 10, 927–940.
Masiokas, M., Rabatel, A., Rivera, A., Ruiz, L., Pitte, P., Ceballos, J., Barcaza, G., Soruco, A., Bown, F., Berthier, E., et al., 2020. A review of the current state and recent changes of the Andean cryosphere. Front. Earth Sci. 8, 99.
Muñoz-Sabater, J., Dutra, E., Agustí-Panareda, A., Albergel, C., Arduini, G., Balsamo, G., Boussetta, S., Choulga, M., Harrigan, S., Hersbach, H., et al., 2021. Era5-land: a state-of-the-art global reanalysis dataset for land applications. Earth Syst.Sci.Data Discuss. 1–50.
Naegeli, K., Huss, M., 2017. Sensitivity of mountain glacier mass balance to changes in bare-ice albedo. Ann. Glaciol. 1–11.
Naegeli, K., Damm, A., Huss, M., Schaepman, M., Hoelzle, M., 2015. Imaging spectroscopy to assess the composition of ice surface materials and their impact on glacier mass balance. Remote Sens. Environ. 168, 388–402.
Naegeli, K., Damm, A., Huss, M., Wulf, H., Schaepman, M., Hoelzle, M., 2017. Cross-comparison of albedo products for glacier surfaces derived from airborne and satellite (sentinel-2 and Landsat 8) optical data. Remote Sens. 9, 110.
Naegeli, K., Huss, M., Hoelzle, M., 2019. Change detection of bare-ice albedo in the Swiss alps. TCry 13, 397–412.
Oerlemans, J., Hoogendoorn, N., 1989. Mass-balance gradients and climatic change. J. Glaciol. 35, 399–405.
Oerlemans, J., Knap, W., 1998. A 1 year record of global radiation and albedo in the ablation zone of Morteratschgletscher, Switzerland. J. Glaciol. 44, 231–238.
Oliveros, V., Morata, D., Aguirre, L., Féraud, G., Fornari, M., 2007. Magmatismo asociado a subducción del jurásico a cretácico inferior en la cordillera de la costa del norte de Chile (18° 30'-24° s): geoquímica y petrogenesis. Rev.Geol.Chile 34, 209–232.
Osmont, D., Wendl, I.A., Schmidely, L., Sigl, M., Vega, C.P., Isaksson, E., Schwikowski, M., 2018. An 800-year high-resolution black carbon ice core record from Lomonosovfonna, Svalbard. Atmos. Chem. Phys. 18, 12777–12795.
Paul, F., Machguth, H., Kääb, A., 2005. On the impact of glacier albedo under conditions of extreme glacier melt: the summer of 2003 in the alps. EARSeL eProc. 4, 139–149.
Paul, F., Kääb, A., Haeberli, W., 2007. Recent glacier changes in the alps observed by satellite: consequences for future monitoring strategies. Glob. Planet. Chang. 56, 111–122.
Paul, F., Machguth, H., Hoelzle, M., Salzmann, N., Haeberli, W., 2008. Alpinewide distributed glacier mass balance modeling. available from the CGIAR-CSI SRTM 90m DatabaseDarkening Peaks: Glacier Retreat, Science, And Society. 111 15.
Pellicciotti, F., Helbing, J., Rivera, A., Favier, V., Corripio, J., Araos, J., Sicart, J.E., Carenzo, M., 2008. A study of the energy balance and melt regime on Juncal Norte Glacier, semi-arid Andes of Central Chile, using melt models of different complexity. Hydrol. Process. 22, 3980–3997.
Peña, M.A., Olmedo, F., 2019. Estimación de las variaciones espacio temporales de albedo en los glaciares Olivares, Chile central. Rev.Geogr.Chile Terra Aust. 55, 35–44.
Pouchou, J.L., Pichoir, F., 1991. Quantitative analysis of homogeneous or stratified microvolumes applying the model "pap". Electron Probe Quantitation. Springer, pp. 31–75.
Ragettli, S., Cortés, G., McPhee, J., Pellicciotti, F., 2014. An evaluation of approaches for modeling hydrological processes in high-elevation, glacierized Andean watersheds. Hydrol. Process. 28, 5674–5695.
RGI, C., 2017. Randolph Glacier Inventory – A Dataset of Global Glacier Outlines: Version 6.0: Technical Report. Digital Media.
Rowe, P.M., Cordero, R.R., Warren, S.G., Stewart, E., Doherty, S.J., Pankow, A., Schrempf, M., Casassa, G., Carrasco, J., Pizarro, J., et al., 2019. Black carbon and other light-absorbing impurities in snow in the Chilean Andes. Sci. Rep. 9, 1–16.
Schaefer, M., Fonseca-Gallardo, D., Farías-Barahona, D., Casassa, G., 2020. Surface energy fluxes on Chilean glaciers: measurements and models. Cryosphere 14, 2545–2565.
Shaw, T.E., Gascoin, S., Mendoza, P.A., Pellicciotti, F., McPhee, J., 2020. Snow depth patterns in a high mountain Andean catchment from satellite optical tristereoscopic remote sensing. Water Resour. Res. 56, e2019WR024880.
Shaw, T.E., Ulloa, G., Farías-Barahona, D., Fernandez, R., Lattus, J.M., McPhee, J., 2021. Glacier albedo reduction and drought effects in the extratropical Andes, 1986–2020. J. Glaciol. 67, 158–169.
Shepherd, G., Terradellas, E., Baklanov, A., Kang, U., Sprigg, K., Nickovic, S., Boloorani, A., Al-Dousari, A., Basart, S., Benedetti, A., et al., 2016. Global Assessment of Sand And Dust Storms. United Nations Environment Programme (UNEP), Nairobi, Kenya 2016.
Shi, Z., Krom, M.D., Bonneville, S., Baker, A.R., Bristow, C., Drake, N., Mann, G., Carslaw, K., McQuaid, J.B., Jickells, T., et al., 2011. Influence of chemical weathering and aging of iron oxides on the potential iron solubility of Saharan dust during simulated atmospheric processing. Glob. Biogeochem. Cycles 25.
Takeuchi, N., Li, Z., 2008. Characteristics of surface dust on Ürümqi Glacier no. 1 in the Tien Shan mountains, China. Arct. Antarct. Alp. Res. 40, 744–750.
Takeuchi, N., Kohshima, S., Seko, K., 2001. Structure, formation, and darkening process of albedo-reducing material (cryoconite) on a Himalayan glacier: a granular algal mat growing on the glacier. Arct. Antarct. Alp. Res. 33, 115–122.
Tapia, J., Davenport, J., Townley, B., Dorador, C., Schneider, B., Tolorza, V., von Tümpling, W., 2018. Sources, enrichment, and redistribution of As, Cd, Cu, Li, Mo, and Sb in the northern Atacama region, Chile: implications for arid watersheds affected by mining. J. Geochem. Explor. 185, 33–51.
Taylor, J., 1991. Computer programs for standardless quantitative analysis of minerals using the full powder diffraction profile. Powder Diffract. 6, 2–9.
Tedesco, M., Doherty, S., Fettweis, X., Alexander, P., Jeyaratnam, J., Stroeve, J., 2016. The darkening of the Greenland ice sheet: trends, drivers, and projections (1981–2100). Cryosphere 10, 477–496. https://doi.org/10.5194/tc-10-477-2016 URL: https://tc.copernicus.org/articles/10/477/2016/.
Tedstone, A.J., Cook, J.M., Williamson, C.J., Hofer, S., McCutcheon, J., Irvine-Fynn, T., Gribbin, T., Tranter, M., 2020. Algal growth and weathering crust state drive variability in western Greenland ice sheet ice albedo. Cryosphere 14, 521–538.
van der Wal, A.C., Das, P., Tigges, A., Becker, A., 1992. Adhesion molecules on the endothelium and mononuclear cells in human atherosclerotic lesions. Am. J. Pathol. 141, 1427.
Vermote, E., Justice, C., Claverie, M., Franch, B., 2016. Preliminary analysis of the performance of the Landsat 8/oli land surface reflectance product. Remote Sens. Environ. 185, 46–56.
Viale, M., Garreaud, R., 2014. Summer precipitation events over the western slope of the subtropical Andes. Mon. Weather Rev. 142, 1074–1092.
Viale, M., Bianchi, E., Cara, L., Ruiz, L.E., Villalba, R., Pitte, P., Masiokas, M., Rivera, J., Zalazar, L., 2019. Contrasting climates at both sides of the Andes in Argentina and Chile. Front.Environ.Sci. 7, 69.
Warren, S.G., 1980. Impurities in snow: effects on albedo. Ann. Glaciol. 5, 177.
Warren, S.G., 1984. Impurities in snow: effects on albedo and snowmelt. Ann. Glaciol. 5, 177–179.
Weidemann, S.S., Sauter, T., Malz, P., Jaña, R., Arigony-Neto, J., Casassa, G., Schneider, C., 2018. Glacier mass changes of lake-terminating grey and Tyndall glaciers at the southern Patagonia icefield derived from geodetic observations and energy and mass balance modeling. Front. Earth Sci. 6, 81.
WGMS, 2021. Fluctuations of Glaciers Database. Technical Report. World Glacier Monitoring Service, Zurich, Switzerland https://doi.org/10.5904/wgms-fog-2021-05.
Wiscombe, W.J., Warren, S.G., 1980. A model for the spectral albedo of snow. I: pure snow. J. Atmos. Sci. 37, 2712–2733.
Wu, G., Xu, T., Zhang, X., Zhang, C., Yan, N., 2016. The visible spectroscopy of iron oxide minerals in dust particles from ice cores on the Tibetan Plateau. Tellus BChem.Phys.Meteorol. 68, 29191.
Zemp, M., Huss, M., Thibert, E., Eckert, N., McNabb, R., Huber, J., Barandun, M., Machguth, H., Nussbaumer, S.U., Gärtner-Roer, I., et al., 2019. Global glacier mass changes and their contributions to sea-level rise from 1961 to 2016. Nature 568, 382–386.
Zhang, Y., Perron, N., Ciobanu, V.G., Zotter, P., Minguillón, M.C., Wacker, L., Prévôt, A.S., Baltensperger, U., Szidat, S., 2012. On the isolation of oc and ec and the optimal strategy of radiocarbon-based source apportionment of carbonaceous aerosols. Atmos. Chem. Phys. 12, 10841–10856.
Zhang, X., Wu, G., Zhang, C., Xu, T., Zhou, Q., 2015. What is the real role of iron oxides in the optical properties of dust aerosols? Atmos. Chem. Phys. 15, 12159–12177.